Geochemistry Geophysics Geosystems G3
AN ELECTRONIC JOURNAL OF THE EARTH SCIENCES
Published by AGU and the Geochemical Society

Article
Volume 9, Number 10
31 October 2008
Q10017, doi:10.1029/2008GC002048
ISSN: 1525-2027

A benchmark study on mantle convection in a 3-D spherical shell using CitcomS

Shijie Zhong
Department of Physics, University of Colorado, Boulder, Colorado 80309, USA (szhong@colorado.edu)

Allen McNamara
School of Earth and Space Exploration, Arizona State University, Tempe, Arizona 85287, USA

Eh Tan
Computational Infrastructure for Geodynamics, California Institute of Technology, Pasadena, California 91125, USA

Louis Moresi
School of Mathematical Sciences, Monash University, Clayton, Victoria 3800, Australia

Michael Gurnis
Seismological Laboratory, California Institute of Technology, Pasadena, California 91125, USA

[1] As high-performance computing facilities and sophisticated modeling software become available, modeling mantle convection in a three-dimensional (3-D) spherical shell geometry with realistic physical parameters and processes becomes increasingly feasible. However, there is still a lack of comprehensive benchmark studies for 3-D spherical mantle convection. Here we present benchmark and test calculations using a finite element code CitcomS for 3-D spherical convection. Two classes of model calculations are presented: the Stokes' flow and thermal and thermochemical convection. For Stokes' flow, response functions of characteristic flow velocity, topography, and geoid at the surface and core-mantle boundary (CMB) at different spherical harmonic degrees are computed using CitcomS and are compared with those from analytic solutions using a propagator matrix method. For thermal and thermochemical convection, 24 cases are computed with different model parameters including Rayleigh number (7×10^3 or 10^5) and viscosity contrast due to temperature dependence (1 to 10^7). For each case, time-averaged quantities at the steady state are computed, including surface and CMB Nussult numbers, RMS velocity, averaged temperature, and maximum and minimum flow velocity, and temperature at the midmantle depth and their standard deviations. For thermochemical convection cases, in addition to outputs for thermal convection, we also quantified entrainment of an initially dense component of the convection and the relative errors in conserving its volume. For nine thermal convection cases that have small viscosity variations and where previously published results were available, we find that the CitcomS results are mostly consistent with these previously published with less than 1% relative differences in globally averaged quantities including Nussult numbers and RMS velocities. For other 15 cases with either strongly temperature-dependent viscosity or thermochemical convection, no previous calculations are available for comparison, but these 15 test calculations from CitcomS are useful for future code developments and comparisons. We also presented results for parallel efficiency for CitcomS, showing that the code achieves 57% efficiency with 3072 cores on Texas Advanced Computing Center's parallel supercomputer Ranger.

Components: 13,962 words, 11 figures, 8 tables.

Keywords: mantle convection; benchmark.

Index Terms: 8121 Tectonophysics: Dynamics: convection currents, and mantle plumes; 8124 Tectonophysics: Earth's interior: composition and state (1212, 7207, 7208, 8105).

Received 5 April 2008; **Revised** 14 August 2008; **Accepted** 5 September 2008; **Published** 31 October 2008.

Zhong, S., A. McNamara, E. Tan, L. Moresi, and M. Gurnis (2008), A benchmark study on mantle convection in a 3-D spherical shell using CitcomS, *Geochem. Geophys. Geosyst.*, *9*, Q10017, doi:10.1029/2008GC002048.

1. Introduction

[2] Mantle convection is the primary mechanism to remove heat from terrestrial planets, thus controlling the thermal evolution of terrestrial planets. Heat transfer and the planform of mantle convection depend critically on the rheology of planetary mantles [*Christensen*, 1984; *Jaupart and Parsons*, 1985; *Moresi and Solomatov*, 1995]. Flow of the Earth's mantle can be characterized as a plate tectonics style of convection in which the highly nonlinear and complicated deformation processes at plate margins play an essential role in causing subduction of lithosphere [*Gurnis*, 1989; *King and Hager*, 1990; *Zhong and Gurnis*, 1996; *Zhong et al.*, 1998; *Moresi and Solomatov*, 1998; *Tackley*, 2000; *Bercovici*, 2003]. However, mantle convection for Mars, Venus, and icy satellites is better characterized as stagnant-lid convection [e.g., *Moresi and Solomatov*, 1995]. Although theoretical analyses on the efficiency of convective heat transfer are available [e.g., *Solomatov*, 1995], numerical modeling of mantle convection has become increasingly important in studying the planform of mantle convection [e.g., *Zhong and Gurnis*, 1993; *Tackley et al.*, 1993; *Bunge et al.*, 1996; *Harder and Christensen*, 1996; *Roberts and Zhong*, 2006; *Zhong et al.*, 2007a] and in incorporating more realistic physical and chemical conditions in the mantle including solid-solid phase changes [e.g., *Christensen and Yuen*, 1984; *Tackley et al.*, 1993; *Sidorin et al.*, 1999], compositionally distinct components [*van Keken et al.*, 1997; *Tackley*, 1998; *McNamara and Zhong*, 2004], and temperature-, stress-, and composition-dependent rheologies [*Moresi and Gurnis*, 1996; *van Hunen et al.*, 2005; *Billen and Hirth*, 2007; *Conrad and Lithgow-Bertelloni*, 2006; *Becker*, 2006].

[3] Significant progress has been made in the last 30 years in developing numerical models of mantle convection in Cartesian domains [*McKenzie et al.*, 1974; *Christensen*, 1984; *King et al.*, 1990; *Tackley*, 1993; *Parmentier et al.*, 1994; *Moresi and Solomatov*, 1995] and in spherical domains [*Young*, 1974; *Baumgardner*, 1985; *Glatzmaier*, 1988; *Zhang and Christensen*, 1993; *Zhang and Yuen*, 1995; *Ratcliff et al.*, 1996a; *Bunge et al.*, 1996; *Zhong et al.*, 2000; *McNamara and Zhong*, 2004; *Yoshida et al.*, 1999; *Yoshida and Kageyama*, 2004; *Oldham and Davies*, 2004; *Harder and Hansen*, 2005; *Stemmer et al.*, 2006; *Choblet et al.*, 2007]. Numerical benchmarks become an important issue, as more modeling packages are developed with more complicated physics. Extensive benchmark studies have been done for Cartesian models of thermal convection [*Blankenbach et al.*, 1989; *Travis et al.*, 1990; *Busse et al.*, 1994; *Moresi and Solomatov*, 1995; *Moresi et al.*, 1996] and thermochemical convection [*van Keken et al.*, 1997; *Tackley and King*, 2003]. However, benchmark studies for spherical shell models of mantle convection are limited to only a small number of cases with either constant or weakly temperature-dependent viscosity [e.g., *Bercovici et al.*, 1989; *Zhang and Christensen*, 1993; *Ratcliff et al.*, 1996a; *Zhong et al.*, 2000; *Richards et al.*, 2002; *Yoshida and Kageyama*, 2004; *Harder and Hansen*, 2005; *Stemmer et al.*, 2006; *Choblet et al.*, 2007].

[4] In this paper, we present numerical benchmark and test calculations using CitcomS for 3-D spherical shell mantle convection with different viscosity parameters (i.e., activation energies), Rayleigh numbers and compositional heterogeneity. Compared with previous studies on spherical shell convection, the current study covers a significantly larger parameter space in Rayleigh number and viscosity parameter and also includes thermochemical convection. Additionally, the current study also includes benchmark calculations for response functions of the geoid anomalies and dynamic topography for CitcomS. Although dynamic topography

benchmark for CitcomS was documented for four different cases in the work of *Zhong et al.* [2000] and calculations for the geoid using CitcomS were tested and presented previously [e.g., *Zhong and Davies*, 1999], the current study is the first to systematically document dynamic topography and geoid benchmarks for CitcomS.

[5] The paper is organized as follows. In section 2, we describe model setups, controlling parameters, initial and boundary conditions, and quantification of model outputs. In section 3, we present benchmark results for response functions of dynamic topography and geoid for Stokes' flow and for thermal and thermochemical convection models. In this section, we also present results for parallel efficiency of CitcomS. In the final section, we discuss our results and present conclusions.

2. Descriptions for Model and Code CitcomS

2.1. Governing Equations

[6] The dynamics of planetary mantles are governed by the conservation of mass, momentum and energy. Under the Boussinesq approximation for an incompressible fluid, including the effects of self-gravitation, the conservation equations are

$$\nabla \cdot \boldsymbol{u} = 0, \tag{1}$$

$$-\nabla p + \nabla \cdot \left[\eta\left(\nabla \boldsymbol{u} + \nabla^T \boldsymbol{u}\right)\right] - (\delta\rho g_0 + \rho_0 \delta g)\boldsymbol{e}_r = 0, \tag{2}$$

$$\rho_0 C_p \left(\frac{\partial T}{\partial t} + \boldsymbol{u} \cdot \nabla T\right) = k\nabla^2 T + \rho_0 H, \tag{3}$$

where $\boldsymbol{u}$ is the velocity in a nonrotating mantle reference frame; p is the dynamic pressure; η, ρ_0, k, and C_p are mantle viscosity, density, thermal conductivity, and specific heat, respectively; g_0, T, and H are gravitational acceleration, temperature, and internal heat generation rate, respectively; t is the time; and $\boldsymbol{e}_r$ is the unit vector in the radial direction. In equation (2), $\delta\rho$ and δg are perturbations to density and radial gravitational acceleration; the last term with δg represents the effect of self-gravitation.

[7] Considering that density perturbations can be due to both thermal expansion and composition, $\delta\rho$ can be expressed as

$$\delta\rho = -\rho_0 \alpha (T - T_0) + \Delta\rho C, \tag{4}$$

where α is the coefficient of thermal expansion, T_0 is the reference temperature and is taken as surface temperature, C is the composition field variable representing compositional heterogeneities, and $\Delta\rho$ is the intrinsic density difference between different composition. For a two-component system that is considered here, C is either 1 or 0.

[8] The perturbation to the radial gravitational acceleration δg is

$$\delta g = -\nabla_r \varphi, \tag{5}$$

where φ is the perturbation to gravitational potential that is determined by the Poisson's equation

$$\nabla^2 \varphi = -4\pi G \delta\rho_{total}, \tag{6}$$

where G is the gravitational constant and $\delta\rho_{total}$ represents density anomalies including that in equation (4) and as well as those associated with the topography at the surface and CMB.

[9] Introduce a reduced pressure P, for example, as *Zhang and Christensen* [1993],

$$P = p - \rho_0 \varphi, \tag{7}$$

and equation (2) can be rewritten as

$$-\nabla P + \nabla \cdot \left[\eta\left(\nabla \boldsymbol{u} + \nabla^T \boldsymbol{u}\right)\right] + [\rho_0 \alpha (T - T_0) - \Delta\rho C] g_0 \boldsymbol{e}_r = 0. \tag{8}$$

[10] The governing equations (1), (8), and (3) are identical in their mathematical form to those with no self-gravitation except that P in equation (8) is interpreted as the reduced pressure which is related to the dynamic pressure p via equation (7). This indicates that self-gravitation in the current formulation using the Boussinesq approximation for an incompressible fluid, does not affect flow velocity and heat transfer.

[11] An equation for transport of composition is

$$\frac{\partial C}{\partial t} + \boldsymbol{u} \cdot \nabla C = 0, \tag{9}$$

[12] The governing equations (1), (8), (3) and (9) can be nondimensionalized as in the work of *Zhong et al.* [2000] using the following normalization schemes:

$$\boldsymbol{r} = R\boldsymbol{r}', \quad t = \frac{R^2}{\kappa} t', \quad \boldsymbol{u} = \frac{\kappa}{R}\boldsymbol{u}', \quad T = \Delta T T' + T_0, \eta = \eta_r \eta', \quad P = \frac{\eta_r \kappa}{R^2} P', \tag{10}$$

where variables with a prime are nondimensional, R is the planetary radius, $\kappa = k/(\rho_0 C_p)$ is the thermal diffusivity, ΔT is the temperature difference between the core-mantle boundary (CMB) and the surface, and η_r is the reference viscosity. The stress scaling is the same as for the pressure.

[13] The nondimensional conservation equations for the mass, momentum and energy and transport equation are

$$\nabla \cdot \boldsymbol{u} = 0, \tag{11}$$

$$-\nabla P + \nabla \cdot \left[\eta\left(\nabla \boldsymbol{u} + \nabla^T \boldsymbol{u}\right)\right] + \xi Ra(T - BC)\boldsymbol{e}_r = 0, \tag{12}$$

$$\frac{\partial T}{\partial t} + \boldsymbol{u} \cdot \nabla T = \nabla^2 T + \gamma, \tag{13}$$

$$\frac{\partial C}{\partial t} + \boldsymbol{u} \cdot \nabla C = 0, \tag{14}$$

where all the variables are non-dimensional with the primes that are dropped, Ra is a Rayleigh number that controls the vigor of convection, $\xi = (R/d)^3$ with d as the mantle thickness, B is a buoyancy number that measures the relative strength between compositional buoyancy and thermal buoyancy, γ is the nondimensional internal heat generation rate, and

$$Ra = \frac{\alpha \rho_0 g_0 \Delta T d^3}{\kappa \eta_r}, \quad B = \frac{\Delta \rho}{\alpha \rho_0 \Delta T}, \quad \gamma = \frac{R^2}{\kappa C_p \Delta T} H. \tag{15}$$

[14] In CitcomS, the planetary radius R is used as the length scale to nondimensionalize the governing equations [*Zhong et al.*, 2000]. While this convention is consistent with that in classical analyses of thermal convection in a spherical shell [e.g., *Chandrasekhar*, 1961], most studies on Earth's mantle convection in a spherical geometry employ the thickness of the mantle d as the length scale [e.g., *Glatzmaier*, 1988]. To follow this convention, we used the same definition of Ra (i.e., equation (15)) by introducing parameter $\xi = (R/d)^3$ in equation (12). In this study, the results for the time and velocity are rescaled using d^2/κ and κ/d as scalings for time and velocity, respectively, unless otherwise specified.

[15] All our model calculations are in a spherical shell geometry with nondimensional inner and outer radii of $r_b = 0.55$ and $r_t = 1$ (i.e., scaled by the planetary radius), respectively, and assume a entirely basal heating (i.e., $\gamma = 0$), and constant material properties except for viscosity.

[16] The viscosity is assumed to be temperature dependent for all the convection calculations. A viscosity parameter, E, which may be equivalent to nondimensional activation energy, controls temperature-dependent viscosity, so that the nondimensional viscosity is given by

$$\eta = \exp[E(0.5 - T)]. \tag{16}$$

This implies that Ra uses viscosity at $T = 0.5$ as the reference viscosity, η_r.

[17] Equations (11) and (12) can be grouped together to define the Stokes' flow problem in which flow velocity and stress fields can be determined for a given buoyancy force and boundary conditions with no explicit involvement of the time [e.g., *Hager and O'Connell*, 1981]. For isochemical convection problems, the relevant governing equations are equations (11)–(13), and composition field variable C and equation (14) are irrelevant. In isochemical convection models there are two controlling parameters, viscosity parameter, E, and Rayleigh number, Ra. For thermochemical models, the composition field variable C and equation (14) become necessary with an additional controlling parameter, buoyancy parameter, B. In this study, we will present calculations for Stokes' flow, isochemical convection, and thermochemical convection using CitcomS.

2.2. Boundary Conditions and Initial Conditions

[18] Boundary conditions are free-slip at the top and bottom boundaries and isothermal with nondimensional temperatures of 0 and 1 at the top and bottom boundaries, respectively (note that temperature boundary conditions are only needed for convection calculations). No flux boundary conditions are used for composition.

[19] For thermal convection or thermochemical convection problems, initial conditions for temperature are needed. Unless otherwise specified, initial conditions for temperature are given as a function of coordinates with perturbations at some given spherical harmonics superimposed on a conductive temperature profile,

$$T(r,\theta,\phi) = \frac{r_b(r - r_t)}{r(r_b - r_t)} + [\varepsilon_c \cos(m\phi) + \varepsilon_s \sin(m\phi)] \cdot p_{lm}(\theta) \sin\left[\frac{\pi(r - r_b)}{(r_t - r_b)}\right], \tag{17}$$

where l and m are spherical harmonic degree and order; r, θ, and φ are radial, colatitude and longitude coordinates; ε_c and ε_s are the magnitudes of perturbation for cosine and sine terms, respectively; and p_{lm} is a normalized associated Legendre polynomial that is related to the associated Legendre polynomial P_{lm} as:

$$p_{lm}(\theta) = \sqrt{\frac{(2l+1)(l-m)!}{2\pi(1+\delta_{m0})(l+m)!}} P_{lm}(\theta). \quad (18)$$

In CitcomS, the normalized associated Legendre polynomial p_{lm} is used as the basis function for spherical harmonic expansion.

[20] The magnitude of the perturbations (i.e., ε_c and ε_s) are 0.01, but for some cases, we only use the cosine term by setting $\varepsilon_s = 0.0$. Perturbations can also include two different sets of harmonics (e.g., $l = 4$, $m = 0$ and $l = 4$, $m = 4$ for all the cubic symmetry cases).

[21] Thermochemical convection models include two components of different intrinsic densities. The dense component is initially placed in the lower layer from the core-mantle boundary at $r_b = 0.55$ to $r_{comp} = 0.775$ (i.e., the middle of the mantle) with no topography at the compositional interface at r_{comp}. Initial temperature for thermochemical convection models is taken from corresponding isochemical convection models. Detailed initial conditions for each case will be discussed later.

2.3 Numerical Solutions of the Governing Equations Using CitcomS

[22] A finite element code for spherical shell mantle convection, CitcomS, is used to solve the conservation equations of the mass, momentum, and energy [*Zhong et al.*, 2000]. Thermochemical convection capability was added by *McNamara and Zhong* [2004] using a particle-ratio method [*Tackley and King*, 2003]. CitcomS employs a non-orthogonal mesh that consists of approximately equal size elements at a given radius and MPI for inter-processor communications [*Zhong et al.*, 2000]. CitcomS was derived from an original serial 3-D Cartesian code Citcom [*Moresi and Solomatov*, 1995; *Moresi and Gurnis*, 1996]. CitcomS employs many similar numerical methods and techniques, compared to its predecessor Citcom. The key features [*Moresi and Solomatov*, 1995; *Zhong et al.*, 2000; *McNamara and Zhong*, 2004; *Zhong et al.*, 2007b] include:

[23] 1. A streamline upwind Petrov Galerkin (SUPG) formulation is used for the energy equation (13) [*Brooks*, 1981; *Hughes*, 2000].

[24] 2. A mixed formulation with primitive variables [e.g., *Hughes*, 2000] and a Uzawa algorithm with two-loop iterations [*Atanga and Silvester*, 1992; *Ramage and Wathen*, 1994; *Moresi and Solomatov*, 1995] are used to solve the mass and momentum equations (11) and (12).

[25] 3. For the Uzawa algorithm, the outer loop iteration for the pressure uses a preconditioned conjugate gradient method, while the inner loop for the velocity uses multigrid [*Moresi and Solomatov*, 1995] and full multigrid [*Zhong et al.*, 2000] methods.

[26] 4. A Gauss-Seidel iteration procedure is used as a smoothing operator for nodes interior to each computational domain or processor, while nodes shared by different processors uses a Jacobi iteration as a smoothing.

[27] 5. A predictor-corrector and second order Runge-Kutte scheme is used to update tracer positions [*Zhong and Hager*, 2003; *McNamara and Zhong*, 2004] and a ratio method is used to project tracer distribution to composition C [*Tackley and King*, 2003]. A scheme for tracing particles in an irregular and non-orthogonal mesh such as in CitcomS was introduced by *McNamara and Zhong* [2004]. The use of a set of regular background mesh in the code is similar to an early implementation of tracing in CitcomS by *van Keken and Zhong* [1999]. For some thermochemical calculations presented in this paper, a computationally more expensive fourth-order Runge-Kutte scheme was also implemented and tested.

[28] The Poisson equation (6) is solved with a spectral method [e.g., *Zhang and Christensen*, 1993; *Zhong and Davies*, 1999]. Suppose that the perturbed gravitational potential φ is only caused by mass anomalies associated with mantle internal density variations $\delta\rho(r, \theta, \phi)$ and with topography at the surface, $s(\theta, \phi)$, and at the CMB, $b(\theta, \phi)$. Applying spherical harmonic expansion to $\delta\rho(r, \theta, \phi)$, $s(\theta, \phi)$ and $b(\theta, \phi)$, all in their dimensional forms, leads to

$$\delta\rho(r,\theta,\phi) = \sum_{l=2}^{N}\sum_{m=0}^{l}\left[\delta\rho_c^{lm}(r)\cos(m\phi) + \delta\rho_s^{lm}(r)\sin(m\phi)\right] \cdot p_{lm}(\theta,\phi), \quad (19)$$

$$s(\theta,\phi)=\sum_{l=2}^{N}\sum_{m=0}^{l}\left[s_c^{lm}\cos(m\phi)+s_s^{lm}\sin(m\phi)\right]p_{lm}(\theta,\phi), \tag{20}$$

$$b(\theta,\phi)=\sum_{l=2}^{N}\sum_{m=0}^{l}\left[b_c^{lm}\cos(m\phi)+b_s^{lm}\sin(m\phi)\right]p_{lm}(\theta,\phi), \tag{21}$$

where subscripts c and s in the expansion coefficients (e.g., b_c^{lm} and b_s^{lm}) are for cosine and sine terms, respectively. In equations (19)–(21), the expansion starts from spherical harmonic degree $l = 2$ because the perturbed gravitational potential at $l = 1$ always vanishes in a reference frame with the planetary center of mass as the center of the reference frame, and N is the highest spherical harmonic degree in the expansion.

[29] The solution for the perturbed potential at spherical harmonic degree l and order m for cosine term, $\varphi_c^{lm}(r)$,

$$\varphi_c^{lm}(r)=\frac{4\pi G}{2l+1}\left[R_{cmb}\left(\frac{R_{cmb}}{r}\right)^{l+1}\Delta\rho_b b_c^{lm}+R\left(\frac{r}{R}\right)^{l}\Delta\rho_t s_c^{lm}+\int_{R_{cmb}}^{R}r'^2\frac{r_<^{l+1}}{\delta}\rho_c^{lm}(r')dr'\right], \tag{22}$$

where all the quantities are in dimensional forms, R_{cmb} and R are the radii of the CMB and surface, respectively, $\Delta\rho_b$ and $\Delta\rho_t$ are the density jumps across the CMB and surface, respectively, $r_< = \min(r', r)$, and $r_> = \max(r', r)$. The solution for the sine term, $\varphi_s^{lm}(r)$, is identical to equation (22) with changing subscripts c to s. Finally, the solution in the spatial domain $\varphi(r, \theta, \phi)$ can be assembled by summing over harmonics as

$$\varphi(r,\theta,\phi)=\sum_{l=2}^{N}\sum_{m=0}^{l}\left[\varphi_c^{lm}(r)\cos(m\phi)+\varphi_s^{lm}(r)\sin(m\phi)\right]\cdot p_{lm}(\theta,\phi). \tag{23}$$

The surface and CMB topography, $s(\theta, \phi)$ and $b(\theta, \phi)$, can be determined from solutions of conservation equations of the mass and momentum [e.g., *Hager and Richards*, 1989]. Calculations of the topography will be discussed later, along with the geoid anomalies.

2.4. Outputs and Modeling Procedures

[30] Two types of benchmark and test calculations are presented in this paper: (1) response functions of dynamic topography and geoid calculations for the Stokes' flow problem, and (2) time-dependent calculations for both isochemical and thermochemical convection. This subsection defines model outputs and modeling procedures.

2.4.1. Nonrotating Reference Frame for the Mantle

[31] Flow velocities in spherical models of mantle convection should be defined in a nonrotating reference frame for the whole mantle [*Zhong*, 2001; *Becker*, 2006]. It is evident from the governing equations that motion of pure rotation (or horizontal translation in Cartesian models with periodic boundary conditions) for the whole mantle affects neither the dynamics nor heat transfer. However, when solving the governing equations numerically, solutions for flow velocities may contain a component of pure rotation for the whole mantle. The cause for such a rotation motion in the numerical solutions is poorly understood, but it is most likely related to numerical solution procedures with no physical meanings. Although it does not affect the physics of heat transfer or deformation, the pure rotation, if existing, may introduce arbitrariness to the flow velocities and affect time stepping for convection problems. Therefore, it is desired that any pure rotation be explicitly removed from the solutions of flow velocities [*Zhong*, 2001].

[32] Here we introduce an efficient procedure to remove the pure rotation from numerical solutions. For a layer of the mantle Ω' with inner and outer radii r_i and r_o, and with a uniform density ρ_0, its pure rotation is described by rotation vector ω. The angular momentum for this layer has the following two equivalent expressions

$$I\omega=\int_{\Omega'}\rho_0 r\times u d\Omega, \tag{24}$$

where $I = 8\pi\rho_0(r_o^5 - r_i^5)/15$ is the moment of inertia for this layer, and r and u are the position and flow velocity vectors, respectively. The rotation vector ω for this layer is

$$\omega=\frac{15}{8\pi\left(r_o^5-r_i^5\right)}\int_{\Omega'}r\times u d\Omega. \tag{25}$$

Equation (25) can be used in both dimensional and non-dimensional calculations.

[33] Applying equation (25) to the whole mantle with $r_o = r_t$ and $r_i = r_b$ yields rotation vector for the whole mantle, ω_o. This pure rotation motion is then removed from the numerical solutions of flow velocities via the following operations

$$\widetilde{\boldsymbol{u}} = \boldsymbol{u} - \boldsymbol{r} \times \omega, \tag{26}$$

or in a spherical coordinate system [e.g., *Zhong*, 2001],

$$\begin{pmatrix} \widetilde{u}_r \\ \widetilde{u}_\theta \\ \widetilde{u}_\phi \end{pmatrix} = \begin{pmatrix} u_r \\ u_\theta - r\omega_o \sin\theta_o \sin(\phi_o - \phi) \\ u_\phi - r\omega_o[\sin\theta\cos\theta_o - \cos\theta\sin\theta_o\cos(\phi_o - \phi)] \end{pmatrix}, \tag{27}$$

where (u_θ, u_ϕ, u_r) are velocity components in colatitudinal, longitudinal, and radial directions; velocities with a tilt are for after removal of the pure rotation motion; and ω_o, θ_o, and φ_o are the magnitude, colatitude, and longitude of the rotation vector ω_o. The flow velocities with removal of the pure rotation motion are then used in determining time step and updating temperature and composition.

[34] We would like to make the following four remarks for the rotation.

[35] 1. In our experience, a pure rotation motion for the whole mantle from the flow solver of CitcomS is often negligibly small for isochemical convection. However, thermochemical calculations appear to show a large component of pure rotation for the whole mantle, and the removal procedure is essential for comparing the velocity field.

[36] 2. A pure rotation, which is sometimes called net rotation or degree-1 toroidal motion, has also been determined via other methods in CitcomS [*Zhong*, 2001; *Becker*, 2006]. The method discussed here that leads to equation (25) is efficient, if the determination of a pure rotation is the sole purpose.

[37] 3. It is possible to remove the pure rotation directly in the Uzawa algorithm, as *Moresi and Solomatov* [1995] did for the original Cartesian version of Citcom with periodic boundary conditions.

[38] 4. Equation (25) can also be applied to any sublayer of the mantle to determine a pure rotation of the sublayer with respect to the nonrotating reference frame of the whole mantle (e.g., the net rotation of the lithosphere). In particular, the net rotation of lithosphere has implications for the reference frame of plate motion [e.g., *O'Connell et al.*, 1991; *Forte and Peltier*, 1994; *Zhong*, 2001; *Becker*, 2006] and seismic anisotropy [*Becker*, 2008].

2.4.2. Dynamic Topography and Geoid from the Stokes' Flow Problem

[39] Benchmark calculations for Stokes' flow are designed to systematically test the accuracy of CitcomS for flow velocity, pressure, dynamic topography, and geoid. The Stokes' flow problem is ideal for benchmarking numerical flow solvers [e.g., *Zhong et al.*, 2000; *Choblet et al.*, 2007], because analytical solutions for the Stokes' flow problems with only radial variations in viscosity can be obtained from a propagator matrix technique [e.g., *Hager and O'Connell*, 1981] and can be used to test numerical codes.

[40] Dynamic topography at the surface, s, with self-gravitation is

$$s = -\frac{\sigma_{rr\_t}}{\Delta\rho_t g_0} = -\frac{\widetilde{\sigma}_{rr\_t} - \rho_0\varphi_t}{\Delta\rho_t g_0}, \tag{28}$$

where φ_t is the perturbed gravitational potential at the surface, σ_{rr_t} is the radial stress at the surface, $\widetilde{\sigma}_{rr\_t}$ is the reduced radial stress at the surface

$$\sigma_{rr\_t} = -p + 2\eta\,\partial u_r/\partial r, \tag{29}$$

$$\widetilde{\sigma}_{rr\_t} = -P + 2\eta\,\partial u_r/\partial r, \tag{30}$$

Notice that when self-gravitation is considered, it is the reduced pressure P rather than the pressure p that is directly solved from the flow solver of CitcomS. Therefore, $\widetilde{\sigma}_{rr\_t}$ is readily calculated from CitcomS. Also, the density difference across the top boundary $\Delta\rho_t$ is equal to the mantle density at the surface ρ_0 if no ocean is assumed at the surface. When an ocean is assumed at the surface, $\Delta\rho_t$ is equal to $\rho_0 - \rho_w$ where ρ_w is the density of water.

[41] Determination of dynamic topography at the CMB, b, differs from that for the surface topography in that the CMB topography depends on assumption of the pressure in the core [e.g., *Zhang and Christensen*, 1993]. With the self-gravitational effect on the core pressure, a Taylor expansion for radial stress at the CMB σ_{rr_b} leads to

$$\sigma_{rr\_b} = \Delta\rho_b g_0 b - \rho_{core}\varphi_b, \tag{31}$$

where φ_b is the perturbed gravitational potential at the CMB, and ρ_{core} is the density of the core at the CMB. Considering equation (7), σ_{rr_b} can be related to the reduced radial stress at the CMB, $\widetilde{\sigma}_{rr\_b}$,

$$\sigma_{rr\_b} = \widetilde{\sigma}_{rr\_b} - \rho_0 \varphi_b. \tag{32}$$

Combining equations (31) and (32) yields

$$b = \frac{\widetilde{\sigma}_{rr\_b} + \Delta\rho_b \varphi_b}{\Delta\rho_b g_0}. \tag{33}$$

[42] Equations (28) and (33) indicate that the surface and CMB topography, s and b, depend on the perturbed gravitational potentials at the surface, φ_t, and CMB, φ_b, respectively, which in principle can be obtained from equation (22) by setting $r = R$ and $r = R_{cmb}$ (i.e., dimensional quantities), respectively. However, φ_t and φ_b also depend on the surface and CMB topography (e.g., equation (22)). Therefore, one needs to couple equations (28) and (33) with equation (22) in the spectral domain (i.e., for each pair of l and m) to simultaneously solve for the topography and perturbed gravitational potentials [e.g., *Zhang and Christensen*, 1993]. The details of this procedure are given in Appendix A.

[43] After the perturbed potential at the surface φ_t is obtained, the geoid anomalies h are readily calculated with

$$h = \varphi_t / g_0. \tag{34}$$

Equation (34) can be used in either the spectral or spatial domain.

2.4.3. Time-Dependent Thermal and Thermochemical Convection Calculations

[44] All the convection cases are computed to a steady state which is defined by insignificant or no variations with time for the averaged surface and bottom heat flux and the volume-averaged temperature and root-mean square (RMS) velocity. The steady state results are then quantified, analyzed, and compared with previous studies when available. Depending on model parameters, each of the isochemical convection cases is computed for between $\sim 10^4$ and $\sim 10^5$ time steps. Thermochemical convection cases will be discussed later.

[45] In each case, we compute, as a function of time, Nussult numbers for both the top and bottom boundaries, Nu_t and Nu_b, averaged temperature for the whole mantle, $\langle T \rangle$ and averaged RMS velocity $\langle V_{rms} \rangle$ for the whole mantle.

$$Nu_t = \frac{r_t (r_t - r_b)}{r_b} Q_t, \tag{35}$$

$$Nu_b = \frac{r_b (r_t - r_b)}{r_t} Q_b, \tag{36}$$

$$\langle T \rangle = \frac{3}{4\pi \left(r_t^3 - r_b^3\right)} \int_{\Omega} T d\Omega, \tag{37}$$

$$\langle V_{rms} \rangle = \left[\frac{3}{4\pi \left(r_t^3 - r_b^3\right)} \int_{\Omega} v^2 d\Omega \right]^{1/2}, \tag{38}$$

where Q_t and Q_b are the surface and bottom heat fluxes, $r_b = 0.55$ and $r_t = 1$, and Ω represents the volume for the whole mantle.

[46] In addition to these global quantities, we also compute the maximum and minimum radial velocity, $V_{r\_md\_\max}$ and $V_{r\_md\_\min}$, and maximum and minimum temperature, T_{md_max} and T_{md_min} at the middle depth of the mantle (i.e., at $r = 0.775$), as computed by *Stemmer et al.* [2006]. When a case reaches a steady state, we then compute the time-averaged values and standard deviations over a certain period of time for Nu_t, Nu_b, $\langle T \rangle$, $\langle V_{rms} \rangle$, $V_{r\_md\_\max}$, $V_{r\_md\_\min}$, $T_{md\_\max}$ and $T_{md\_\min}$.

[47] For thermochemical convection calculations, we add two additional measures, the relative error in conserving the total volume of the dense component ε_v and the volume of entrained dense component in the upper layer C_e:

$$\varepsilon_V = \left[\int_{\Omega} C(t) d\Omega - \int_{\Omega} C(0) d\Omega \right] \Big/ \int_{\Omega} C(0) d\Omega, \tag{39}$$

$$C_e = \int_{\Omega'} C(t) d\Omega, \tag{40}$$

where Ω represents the volume for the whole mantle and Ω' is for a layer with inner radius of $r_{comp} + 0.1$ and outer radius of r_t, and $C(0)$ and $C(t)$ are composition initially and at time t. Note that the dense layer is represented with $C = 1$. C_e measures entrainment of the dense component from the bottom to the top layers [e.g., *van Keken et al.*, 1997].

Table 1. CPU Time With Different Number of Cores

N_c[a]	Total Time (s)	Time for Zeroth Step (s)	Iterations[b]	Time Per v Iteration (s)	Efficiency (%)
12(1 × 1 × 1)	69.8	9.3	112(118)	0.59	100
24(1 × 1 × 2)	64.1	9.8	95(103)	0.62	95
48(2 × 2 × 1)	53.7	9.7	73(78)	0.69	86
96(2 × 2 × 2)	53.9	8.8	74(79)	0.68	87
192(4 × 4 × 1)	47.2	11.3	55(63)	0.75	79
384(4 × 4 × 2)	46.8	8.2	55(58)	0.81	73
768(4 × 4 × 4)	52.4	10.0	58(61)	0.86	69
1536(8 × 8 × 2)	58.2	16.0	60(70)	0.83	71
3072(8 × 8 × 8)	59.1	17.5	54(57)	1.04	57

[a] N_c stands for the number of core. The numbers in the parentheses represent the domain decomposition in each of 12 spherical caps for CitcomS. For example, 2 × 2 × 2 indicates that each cap is further divided into two in each of the three directions with the last number for the radial direction.
[b] The numbers in and out of the parentheses represent the numbers of inner loop velocity iteration and of outer loop pressure iteration, respectively.

2.5. Parallel Efficiency

[48] Before presenting results from benchmark and test calculations, we show in this subsection parallel efficiency for CitcomS. Parallel computing in CitcomS is enabled by MPI for interprocessor communications, and *Zhong et al.* [1998, 2000] discussed the MPI implementations in Citcom family of codes. For parallel efficiency calculations, we computed an isoviscous thermal convection problem for 50 time steps using different number of cores (i.e., processors) ranging from 12 to 3072 cores on Taxes Advanced Computing Center's parallel supercomputer Ranger. For each calculation, the total number of elements increases linearly with the number of cores with the number of element per core fixed at 32^3. The error tolerance was set to be 10^{-2} (i.e., for each time step, the Stokes flow solve terminates when the relative difference in either velocity or pressure solutions is less than 1%).

[49] Table 1 shows for each test calculation the CPU time in seconds for the initial Stokes flow solve and 50 time steps and also the total numbers of outer loop pressure iterations and inner loop velocity iterations (i.e., full multigrid cycles). Significantly more iterations are needed for the initial Stokes flow solve than for subsequent time steps. While the CPU time for the 50 time steps of calculation varies from 69.8 s with 12 cores to 59.1 s with 3072 cores, its minimum of 46.8 s occurs with 384 cores (Table 1). The difference in CPU time is directly related to the number of outer loop and inner loop iterations. Because the number of elements (i.e., velocity and pressure unknowns) varies with the number of cores, the numbers of outer loop and inner loop iterations may also vary. Therefore, our results here reflect not only parallel scalability but also algorithmic scalability. We determined a parallel efficiency (i.e., scalability) using CPU time per inner loop velocity iterations, and the efficiency is 71% for 1536 cores and 57% for 3072 cores (Table 1). However, it should be pointed out that the parallel efficiency given here may depend on a number of other factors including mesh size per core, domain decomposition, and error tolerance.

3. Results

3.1. Benchmark Calculations for the Stokes' Flow

[50] This study significantly extends the Stokes' flow benchmark in the work of *Zhong et al.* [2000] by including calculations for wavelengths down to $l = 15$ (only computed to $l = 4$ previously) and buoyancy forces at different depths, the effects of self-gravitation in the geoid and dynamic topography calculations, and a consistent boundary flux (CBF) method for determining the radial stresses at the top and bottom boundaries [*Zhong et al.*, 1993].

3.1.1. Definition of Benchmark Calculations for the Stokes' Flow

[51] Similar to calculations of response functions for the geoid and topography [e.g., *Hager and Richards*, 1989], our benchmark calculations for Stokes' flow assume either isovicous or depth-dependent viscosity, and a buoyancy confined at different depths and at different spherical harmonic degrees [*Zhong et al.*, 2000; *Choblet et al.*, 2007]. Solutions to the Stokes' flow problem are determined from both the propagator matrix method and

CitcomS and are compared using flow velocity, dynamic topography, and the geoid at the top and bottom boundaries.

[52] The buoyancy is specified as a delta function in the radial direction and spherical harmonic function in horizontal directions,

$$\delta\rho(r,\theta,\phi) = \sigma_0 \delta(r - r_0)\cos(m\phi)p_{lm}(\theta), \tag{41}$$

where σ_0 is a surface density, r_0 is the radial location of the buoyancy force, and only cosine term is considered in the longitudinal direction.

[53] For each calculation with a given buoyancy (i.e., r_0, l, and m), we compute nondimensional topography and geoid at the surface and CMB. Additionally, we also compute characteristic horizontal velocity, U, and divergence of horizontal velocities, $\nabla_h \cdot \boldsymbol{u}$, for the top and bottom boundaries, where

$$\nabla_h \cdot u = \frac{\partial u_\theta}{r\partial\theta} + \frac{u_\theta \cot\theta}{r} + \frac{1}{r\sin\theta}\frac{\partial u_\phi}{\partial\phi}, \tag{42}$$

and U is given such that [e.g., *Hager and O'Connell*, 1981]

$$u_\theta = U\frac{\partial Y_{lm}(\theta,\phi)}{r\partial\theta}, \quad u_\phi = \frac{U}{r\sin\theta}\frac{\partial Y_{lm}(\theta,\phi)}{\partial\phi}, \tag{43}$$

where Y_{lm} represents any form of spherical harmonic functions. U is a function of spherical harmonic degree l and radial coordinate r.

[54] For the Stokes' flow problem with buoyancy given in (41), it is appropriate to use the stress scale $\sigma_0 g$ to nondimensionalize stress. Accordingly, $\sigma_0/\Delta\rho_t$ and $\sigma_0/\Delta\rho_b$ are used as scales for the surface and CMB topography, respectively, and $4\pi GR\sigma_0/g$ and $\sigma_0 gR/\eta_r$ are scales for the geoid and velocity, respectively (Appendix A). The procedures for determining these nondimensional quantities, along with relevant parameters used in the calculations, are given in Appendix A.

[55] In calculations with CitcomS, the buoyancy structure can be specified in CitcomS by setting $B = 0$, $\xi Ra = 1$ in (12), and

$$T(r,\phi,\theta) = \delta(r - r_0)\cos(m\phi)p_{lm}(\theta). \tag{44}$$

For most Stokes' flow benchmark calculations, a mesh with 12 × (64 × 64 × 64) elements (i.e., in each of 12 subdivisions of a spherical shell, 64 elements are used in the radial, and two horizontal directions; see *Zhong et al.* [2000]) is used. The delta function in (41) and (44) is approximated as

$$\delta(r - r_0) = \begin{cases} \dfrac{n_{er}}{r_t - r_b}, & r = r_0 \\ 0, & otherwise \end{cases}, \tag{45}$$

where $n_{er} = 64$ is the number of elements in the radial direction and a uniform grid is used in the radial direction. Equation (45) preserves the integral property of the delta function.

[56] While determinations of stress (i.e., via a CBF method), topography, and velocity divergence at the surface and CMB are straightforward in CitcomS, the characteristic horizontal velocity, U, at the surface and CMB, which is defined in the spherical harmonic domain (e.g., equation (43)), can be determined via the following relation

$$U^2 = \frac{1}{l(l+1)}\oint_A \left(u_\theta^2 + u_\phi^2\right)\sin\theta d\theta d\phi, \tag{46}$$

where the velocities in the integrand are on the finite element grid from CitcomS at a relevant radius (i.e., either at the surface or CMB) and the integral is only for coordinates θ and φ but covers the entire spherical surface A. Equation (46) follows from the orthogonal properties of spherical harmonic functions [*Dahlen and Tromp*, 1998].

3.1.2. Benchmark Results for the Stokes' Flow

[57] The first set of benchmark calculations assumes a uniform viscosity. The radial dependences of response functions of surface and CMB topography, geoid, characteristic horizontal velocities, and velocity divergences determined from both propagator matrix solution method and CitcomS are shown for $l = 2$, 5, 8, and 15 in Figure 1. The response functions at three different depths of d/4, d/2, and 3d/4 from these two different methods are also presented in Table 2. The general results are similar to those in the work of *Hager and Richards* [1989]. For example, when the buoyancy force is located at the surface (CMB), the topography at the surface (CMB) is equal to unity but zero at the CMB (surface), and flow velocity is zero at both boundaries. Comparisons between solutions from the propagator matrix method (solid lines in Figure 1) and CitcomS (dashed lines) indicate that CitcomS reproduces the propagator matrix solutions well. Relative errors are generally about 1% or less (Table 2). Although these calcu-

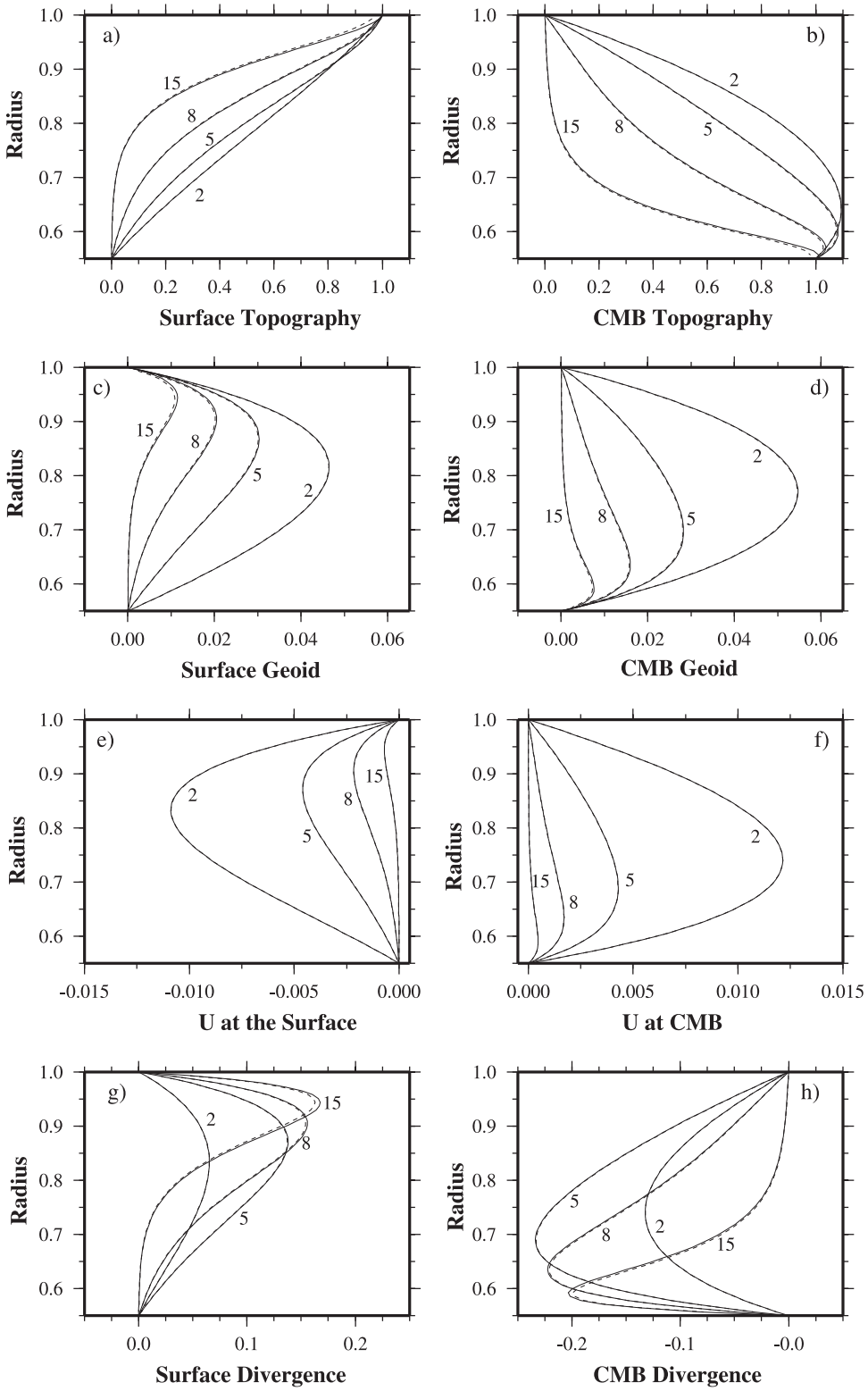

Figure 1. Radial dependences of response functions of (a) surface topography, (b) core-mantle boundary (CMB) topography, (c) surface geoid, (d) CMB geoid, characteristic velocity at (e) the surface, and (f) CMB, and divergence of velocity at (g) the surface and (h) CMB for spherical harmonic degrees 2, 5, 8, and 15 from analytic (solid lines) and CitcomS (dashed lines) solutions for the first set (i.e., uniform viscosity) of the Stokes' flow benchmarks.

Table 2. Response Functions for the First Set of Calculations of the Stokes' Flow[a]

Depth	l	s	b	h_t	h_b	U_t	U_b	$\nabla \cdot V_t$	$\nabla \cdot V_b$
0.25d	2	7.712e-01	5.639e-01	4.047e-02	4.051e-02	−9.941e-03	7.707e-03	5.966e-02	−8.408e-02
		(7.716e-01)	(5.646e-01)	(4.058e-02)	(4.062e-02)	(−9.949e-03)	(7.709e-03)	(5.969e-02)	(−8.410e-02)
	5	7.537e-01	3.879e-01	2.963e-02	1.547e-02	−4.540e-03	2.133e-03	1.359e-01	−1.160e-01
		(7.562e-01)	(3.894e-01)	(2.986e-02)	(1.556e-02)	(−4.546e-03)	(2.134e-03)	(1.364e-01)	(−1.164e-01)
	8	6.407e-01	1.613e-01	1.988e-02	4.397e-03	−2.124e-03	4.469e-04	1.518e-01	−5.797e-02
		(6.458e-01)	(1.629e-01)	(2.018e-02)	(4.454e-03)	(−2.128e-03)	(4.480e-04)	(1.532e-01)	(−5.865e-02)
	15	3.797e-01	1.047e-02	8.007e-03	1.654e-04	−5.045e-04	1.026e-05	1.178e-01	−4.327e-03
		(3.905e-01)	(1.094e-02)	(8.355e-03)	(1.739e-04)	(−5.074e-04)	(1.044e-05)	(1.218e-01)	(−4.557e-03)
0.5d	2	4.991e-01	9.302e-01	4.469e-02	5.446e-02	−1.006e-02	1.186e-02	6.035e-02	−1.294e-01
		(4.998e-01)	(9.313e-01)	(4.486e-02)	(5.461e-02)	(−1.006e-02)	(1.186e-02)	(6.038e-02)	(−1.294e-01)
	5	4.226e-01	7.209e-01	2.415e-02	2.529e-02	−3.591e-03	3.733e-03	1.074e-01	−2.030e-01
		(4.238e-01)	(7.235e-01)	(2.427e-02)	(2.543e-02)	(−3.593e-03)	(3.733e-03)	(1.078e-01)	(−2.036e-01)
	8	2.658e-01	3.760e-01	1.109e-02	9.362e-03	−1.168e-03	9.883e-04	8.342e-02	−1.283e-01
		(2.679e-01)	(3.794e-01)	(1.122e-02)	(9.474e-03)	(−1.170e-03)	(9.890e-04)	(8.427e-02)	(−1.295e-01)
	15	6.686e-02	5.342e-02	1.733e-03	8.022e-04	−1.080e-04	5.035e-05	2.518e-02	−2.125e-02
		(6.905e-02)	(5.554e-02)	(1.804e-03)	(8.399e-04)	(−1.091e-04)	(5.095e-05)	(2.618e-02)	(−2.223e-02)
0.75d	2	2.320e-01	1.089	2.780e-02	4.249e-02	−5.486e-03	1.044e-02	3.290e-02	−1.140e-01
		(2.323e-01)	(1.090)	(2.788e-02)	(4.267e-02)	(−5.486e-03)	(1.046e-02)	(3.291e-02)	(−1.141e-01)
	5	1.660e-01	1.005	1.138e-02	2.723e-02	−1.600e-03	4.200e-03	4.784e-02	−2.287e-01
		(1.664e-01)	(1.008)	(1.143e-02)	(2.741e-02)	(−1.600e-03)	(4.201e-03)	(4.801e-02)	(−2.292e-01)
	8	7.570e-02	7.410e-01	3.605e-03	1.522e-02	−3.699e-04	1.636e-03	2.641e-02	−2.127e-01
		(7.634e-02)	(7.471e-01)	(3.644e-03)	(1.542e-02)	(−3.707e-04)	(1.637e-03)	(2.669e-02)	(−2.143e-01)
	15	7.019e-03	2.916e-01	1.974e-04	3.863e-03	−1.219e-05	2.441e-04	2.839e-03	−1.034e-01
		(7.289e-03)	(3.006e-01)	(2.061e-04)	(4.023e-03)	(−1.238e-05)	(2.453e-04)	(2.973e-03)	(−1.071e-01)

[a]Note: s, b, h_t, h_b, U_t, U_b, $\nabla \cdot V_t$, and $\nabla \cdot V_b$ are surface and CMB topographies, surface and CMB geoid, surface and CMB characteristic velocities, and surface and CMB velocity divergence, respectively. The numbers in parentheses are analytical solutions. We use the notation that 4e-4 represents 4×10^{-4}.

lations are for $m = 0$, CitcomS calculations with nonzero m show nearly identical relative errors.

[58] The second set of calculations differ from the first only in having a layered viscosity structure in which the top 179.156 km (i.e., four elements) of the mantle has a viscosity 10^4 times higher than the layer below. The results from CitcomS again agree well with those from the propagator matrix method for this set of calculations with large radial viscosity variations (Figure 2 and Table 3). Notice that with the high-viscosity top layer, the response functions for characteristic horizontal velocity and velocity divergence at the surface are nearly zero, regardless of the depth of the buoyancy force (Figures 2e and 2g).

[59] We also compute the response functions with no self-gravitational effects. As pointed out earlier, self-gravitational effects do not affect flow velocity. However, they affect interpretations of the pressure in equations (12) and (7) (i.e., the reduced pressure versus pressure) and definitions of dynamic topography in equations (28) and (31) and geoid. More specifically, with no self-gravitation, we need to remove the $\rho_0 \delta g$ term from equation (2) and the gravitational potential terms from equations (7), (28), and (31). Figure 3 compares the response functions of surface and CMB topography and geoid from CitcomS and the propagator matrix method solutions for both isoviscous (Figures 3a–3d) and layered viscosity (Figures 3e–3h) models. Table 4 shows the results at the depth of d/2 for both isoviscous and layered viscosity calculations with no self-gravitation. It is clear that self-gravitation causes relatively large difference for topography and geoid at low spherical harmonics or long-wavelengths (Figures 1–3). These results suggest that CitcomS reproduces the propagator matrix method solutions well with similar accuracy to that with self-gravitational effects.

[60] It is worthwhile to point out that including self-gravitational effects on topography and geoid does not add any additional solution cost for Stokes' flow, compared to that without the effect. This is because self-gravitation only affects the interpretation of pressure in the momentum equation. Therefore, self-gravitation can be accounted for as a postprocessing process in the Stokes' flow modeling.

[61] We now present resolution tests to examine convergence of the benchmarks. For the first set of benchmark calculations with a uniform viscosity structure, the response functions at depths of d/4, d/2 and 3d/4 are computed at three other numerical resolutions: $12 \times (24 \times 24 \times 24)$, $12 \times (32 \times 32 \times 32)$, and $12 \times (48 \times 48 \times 48)$. In general, relative errors of response functions from CitcomS calculations decrease with increasing resolution (Figures 4a and 4b for the errors of the surface and CMB response functions at a depth of d/2 and $l = 5$, respectively). A number of general conclusions can be drawn from these results about relative errors.

[62] 1. The relative errors for all the response functions decrease approximately as the square of numerical resolution, suggesting that the response function calculations from CitcomS are second order accurate. This result is interesting but needs to be better understood, because with the linear elements used in CitcomS, while the velocity field is expected to be second-order accurate, topography and divergence that are related to the derivatives of velocity are expected to be first-order accurate.

[63] 2. The relative errors for the response functions of the geoid are larger than those for other response functions. This is because the geoid results from subtraction of contributions from the buoyancy and topography which are comparable in amplitudes but are much larger than the geoid itself.

[64] 3. The relative errors for horizontal characteristic velocity are the smallest.

[65] The relative errors for the surface response functions (Figure 4a) show similar behaviors to those for the CMB response functions (Figure 4b). The errors for longer wavelength response functions are also smaller than those for shorter wavelengths (Figures 4c and 4d for $l = 2$ and $l = 15$, respectively). The relative errors for the surface response functions appear to be larger at shallower depths (Figures 4e and 4f for depths of 3d/4 and d/4, respectively).

3.2. Calculations for Thermal and Thermochemical Convection

3.2.1. Thermal Convection

[66] Two sets of total 22 cases are presented here, one associated with tetrahedral symmetry and the other with cubic symmetry. Ra ranges from $7 \times$

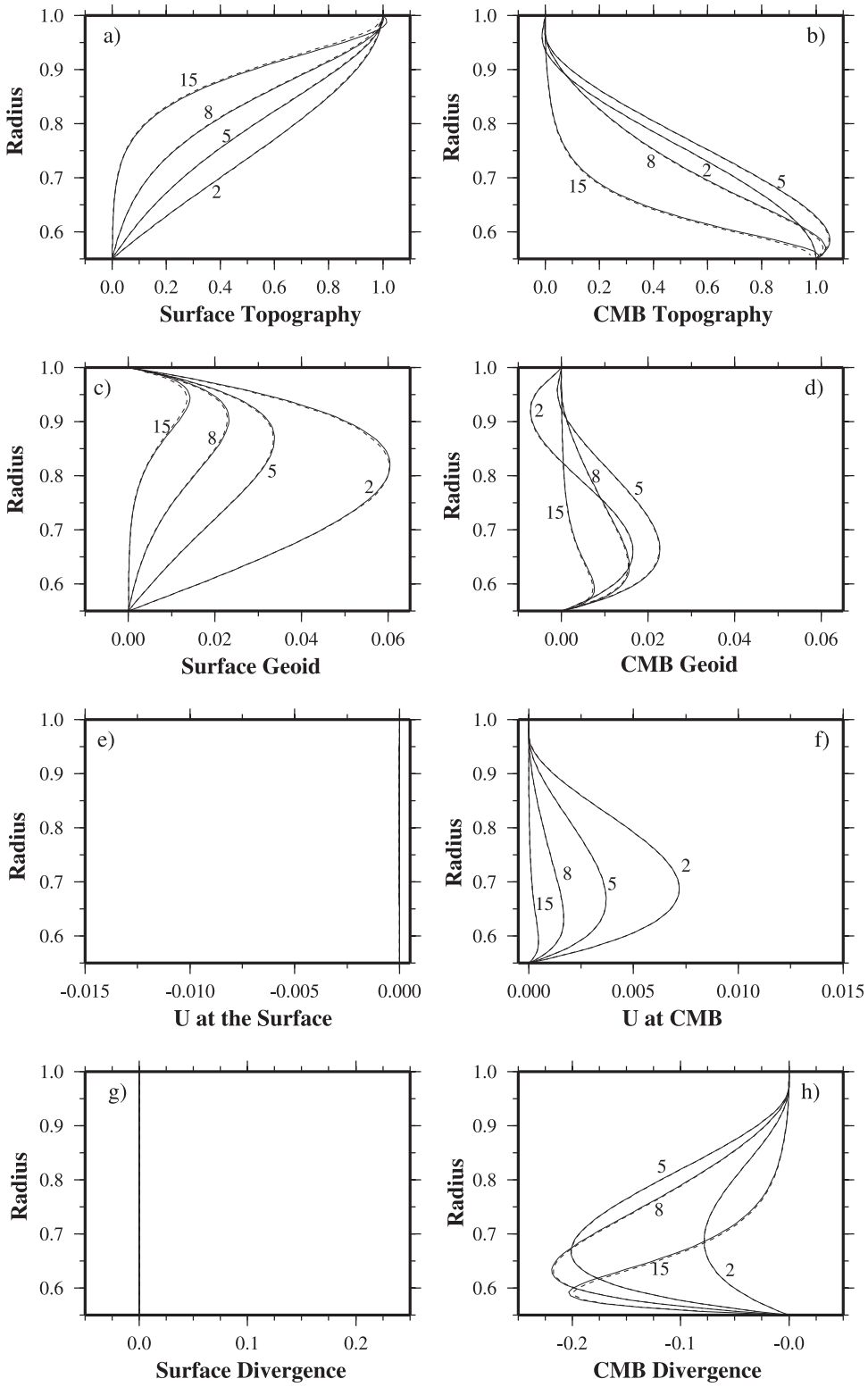

Figure 2. Same as in Figure 1 but for the second set (i.e., layered viscosity) of the Stokes' flow benchmarks.

Table 3. Response Functions for the Second Set of Calculations of the Stokes' Flow[a]

Depth	l	s	b	h_t	h_b	U_t	U_b	$\nabla \cdot V_t$	$\nabla \cdot V_b$
0.25d	2	8.774e-01	7.981e-02	5.286e-02	−6.307e-03	−1.228e-05	1.547e-03	7.360e-05	−1.688e-02
		(8.798e-01)	(7.981e-02)	(5.333e-02)	(−6.165e-03)	(−1.231e-05)	(1.543e-03)	(7.384e-05)	(−1.683e-02)
	5	7.952e-01	1.250e-01	3.304e-02	2.513e-03	−1.961e-06	7.100e-04	5.860e-05	−3.861e-02
		(7.976e-01)	(1.254e-01)	(3.326e-02)	(2.543e-03)	(−1.964e-06)	(7.093e-04)	(5.893e-05)	(−3.869e-02)
	8	6.859e-01	7.893e-02	2.253e-02	1.756e-03	−6.491e-07	2.192e-04	4.629e-05	−2.844e-02
		(6.913e-01)	(7.955e-02)	(2.284e-02)	(1.778e-03)	(−6.509e-07)	(2.191e-04)	(4.687e-05)	(−2.869e-02)
	15	4.379e-01	8.042e-03	9.885e-03	1.226e-04	−1.096e-07	7.858e-06	2.547e-05	−3.314e-03
		(4.501e-01)	(8.396e-03)	(1.028e-02)	(1.290e-04)	(−1.103e-07)	(7.999e-06)	(2.647e-05)	(−3.490e-03)
0.5d	2	6.102e-01	4.350e-01	5.784e-02	6.701e-03	−1.258e-05	5.556e-03	7.543e-05	−6.064e-02
		(6.104e-01)	(4.354e-01)	(5.789e-02)	(6.754e-03)	(−1.258e-05)	(5.556e-03)	(7.549e-05)	(−6.061e-02)
	5	4.552e-01	5.093e-01	2.682e-02	1.487e-02	−1.574e-06	2.588e-03	4.703e-05	−1.407e-01
		(4.567e-01)	(5.110e-01)	(2.696e-02)	(1.496e-02)	(−1.577e-06)	(2.587e-03)	(4.730e-05)	(−1.411e-01)
	8	2.904e-01	3.294e-01	1.253e-02	7.867e-03	−3.645e-07	8.591e-04	2.598e-05	−1.115e-01
		(2.928e-01)	(3.323e-01)	(1.268e-02)	(7.963e-03)	(−3.654e-07)	(8.598e-04)	(2.631e-05)	(−1.126e-01)
	15	7.913e-02	5.287e-02	2.129e-03	7.925e-04	−2.416e-08	4.974e-05	5.593e-06	−2.099e-02
		(8.166e-02)	(5.497e-02)	(2.211e-03)	(8.298e-04)	(−2.436e-08)	(5.040e-05)	(5.846e-06)	(−2.199e-02)
0.75d	2	2.930e-01	8.186e-01	3.506e-02	1.645e-02	−6.881e-06	7.007e-03	4.125e-05	−7.653e-02
		(2.927e-01)	(8.192e-01)	(3.500e-02)	(1.650e-02)	(−6.879e-06)	(7.009e-03)	(4.127e-05)	(−7.646e-02)
	5	1.804e-01	9.098e-01	1.257e-02	2.256e-02	−7.047e-07	3.688e-03	2.105e-05	−2.008e-01
		(1.811e-01)	(9.128e-01)	(1.263e-02)	(2.272e-02)	(−7.054e-07)	(3.688e-03)	(2.116e-05)	(−2.012e-01)
	8	8.339e-02	7.262e-01	4.055e-03	1.474e-02	−1.159e-07	1.596e-03	8.263e-06	−2.074e-01
		(8.421e-02)	(7.321e-01)	(4.105e-03)	(1.493e-02)	(−1.164e-07)	(1.596e-03)	(8.384e-06)	(−2.089e-01)
	15	8.401e-03	2.915e-01	2.419e-04	3.862e-03	−5.884e-09	2.441e-04	6.371e-07	−1.033e-01
		(8.713e-03)	(3.006e-01)	(2.520e-04)	(4.022e-03)	(−2.789e-09)	(2.453e-04)	(6.693e-07)	(−1.070e-01)

[a] Note: See Table 2 for notations.

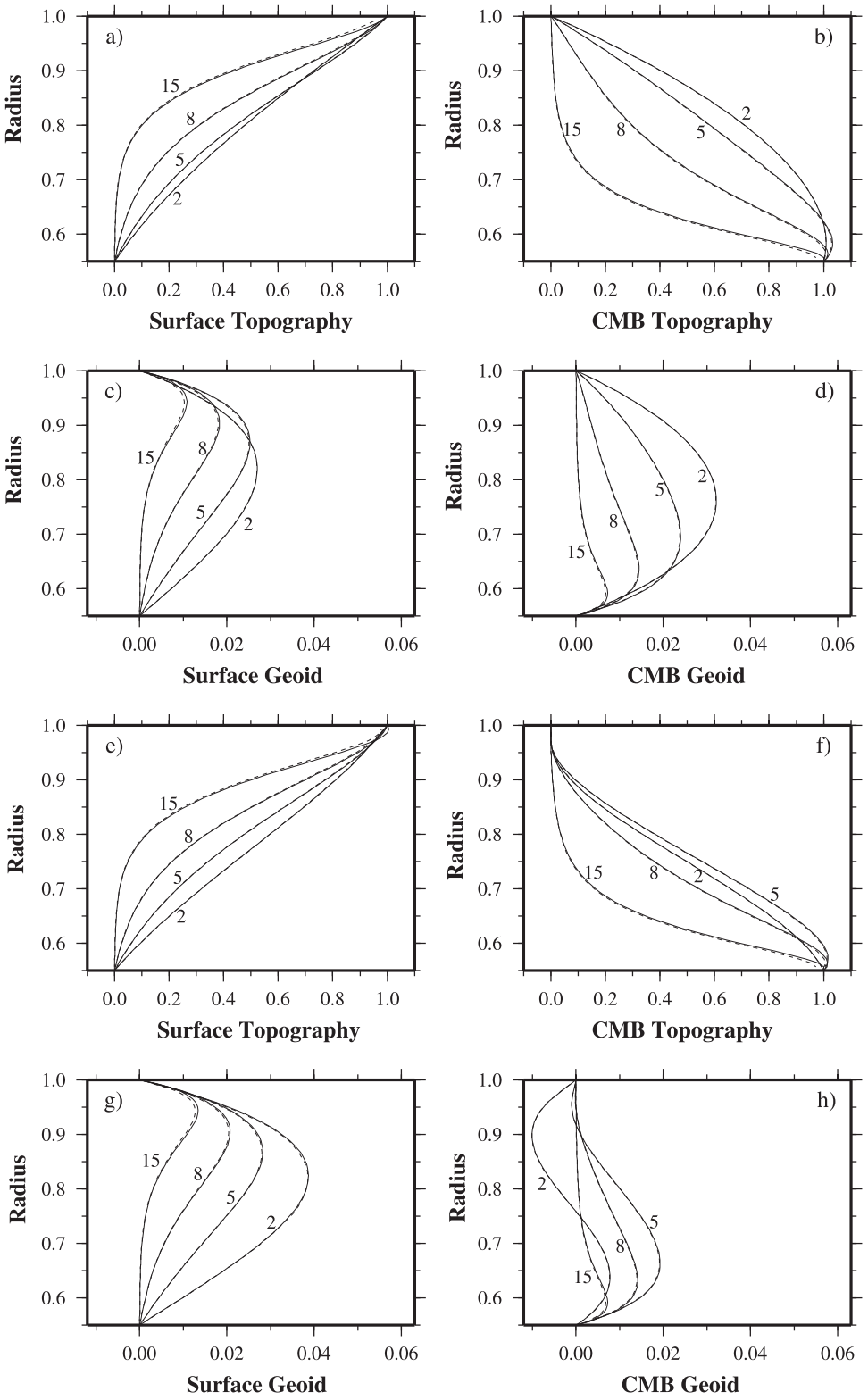

Figure 3. Radial dependences of response functions of (a) surface topography, (b) CMB topography, (c) surface geoid, and (d) CMB geoid for spherical harmonic degrees 2, 5, 8, and 15 from analytic (solid lines) and CitcomS (dashed lines) solutions for the first set of the Stokes' flow benchmarks with no self-gravitational effects. (e, f, g, and h) The corresponding results for the second set of the Stokes' flow benchmarks with no self-gravitational effects.

Table 4. Response Functions at a Depth of 0.5*d* for the Stokes' Flow With no Self-Gravitational Effects[a]

Set	l	s	b	h_t	h_b	U_t	U_b	$\nabla \cdot V_t$	$\nabla \cdot V_b$
1	2	4.187e-01	7.700e-01	2.568e-02	3.196e-02	−1.006e-02	1.186e-02	6.035e-02	−1.294e-01
		(4.192e-01)	(7.706e-01)	(2.579e-02)	(3.206e-02)	(−1.006e-02)	(1.186e-02)	(6.038e-02)	(−1.294e-01)
	5	3.791e-01	6.464e-01	2.009e-02	2.137e-02	−3.591e-03	3.733e-03	1.074e-01	−2.030e-01
		(3.802e-01)	(6.487e-01)	(2.020e-02)	(2.149e-02)	(−3.593e-03)	(3.733e-03)	(1.078e-01)	(−2.036e-01)
	8	2.458e-01	3.484e-01	9.913e-03	8.461e-03	−1.168e-03	9.883e-04	8.342e-02	−1.282e-01
		(2.478e-01)	(3.516e-01)	(1.003e-02)	(8.563e-03)	(−1.170e-03)	(9.890e-04)	(8.427e-02)	(−1.295e-01)
	15	6.374e-02	5.106e-02	1.633e-03	7.603e-04	−1.080e-04	5.035e-05	2.518e-02	−2.125e-02
		(6.581e-02)	(5.307e-02)	(1.699e-03)	(7.961e-04)	(−1.091e-04)	(5.095e-05)	(2.618e-02)	(−2.223e-02)
2	2	5.061e-01	4.153e-01	3.667e-02	−1.763e-03	−1.258e-05	5.556e-03	7.543e-05	−6.064e-02
		(5.063e-01)	(4.155e-01)	(3.671e-02)	(−1.729e-03)	(−1.258e-05)	(5.556e-03)	(7.549e-05)	(−6.061e-02)
	5	4.070e-01	4.656e-01	2.238e-02	1.246e-02	−1.574e-06	2.588e-03	4.703e-05	−1.407e-01
		(4.082e-01)	(4.670e-01)	(2.249e-02)	(1.253e-02)	(−1.577e-06)	(2.587e-03)	(4.730e-05)	(−1.411e-01)
	8	2.679e-01	3.063e-01	1.121e-02	7.107e-03	−3.645e-07	8.591e-04	2.598e-05	−1.115e-01
		(2.700e-01)	(3.089e-01)	(1.133e-02)	(7.194e-03)	(−3.654e-07)	(8.598e-04)	(2.631e-05)	(−1.126e-01)
	15	7.530e-02	5.054e-02	2.006e-03	7.511e-04	−2.416e-08	4.974e-05	5.593e-06	−2.099e-02
		(7.769e-02)	(5.253e-02)	(2.083e-03)	(7.865e-04)	(−2.436e-08)	(5.040e-05)	(5.846e-06)	(−2.199e-02)

[a] Note: See Table 2 for notations. These results are for a depth of 0.5*d* only.

10^3 to 10^5 and viscosity variations due to its temperature-dependence, $\Delta\eta$ = exp(E), ranges from 1 (i.e., isoviscous) for mobile-lid convection to 10^7 for stagnant lid convection (Table 5). For cases with $Ra = 7 \times 10^3$, we use $12 \times (32 \times 32 \times 32)$ elements, and for cases with $Ra = 10^5$, $12 \times (48 \times 48 \times 48)$ elements are used. Radial resolution is refined in the top and bottom boundary layers such that the resolution there is about twice of other regions.

3.2.1.1. Cases With Tetrahedral Symmetry and its Variations

[67] For all the cases in this set, $Ra = 7 \times 10^3$ is used, but they have different temperature-dependent viscosity with $\Delta\eta$ of 1, 10, 20, 10^2, 10^3, 10^4, 10^5, 10^6, and 10^7 (Cases A1–A9 in Table 5 for definitions of these cases). The initial condition is the same for these cases with $\varepsilon_c = \varepsilon_s = 0.01$ and $l = 3$ and $m = 2$ in equation (17). The first three cases, A1–A3, were also presented by *Stemmer et al.* [2006], *Ratcliff et al.* [1996a], and *Yoshida and Kageyama* [2004], while *Bercovici et al.* [1989] and *Zhong et al.* [2000] computed just case A1. All these cases are computed to a steady state; the time dependences of $\langle T \rangle$, $\langle V_{rms} \rangle$, and Nu_t for three different cases are shown in Figures 5a–5c, respectively. In general, cases with large $\Delta\eta$ require more time steps to reach a steady state (Table 5). Only the first five cases, A1–A5, display tetrahedral symmetry in steady states (Figures 6a–6c). The last three cases, A7–A9 are in stagnant-lid convection regime, with a large number of small plumes at depth (Figures 6e and 6f) [*Tackley*, 1993; *Ratcliff et al.*, 1996b]. Case A6 with $\Delta\eta$ of 10^4 is a transitional case that shows convective planform with much longer wavelengths; the planform is largely spherical harmonic degree-1 (Figure 6d). The steady state radial dependence of horizontally averaged temperature and RMS velocity (Figures 7a and 7b) further confirm that cases A7–A9 with their negligibly small flow velocity near the surface and high interior temperature are in stagnant-lid convection regime.

[68] Table 6 shows time-averaged steady state results of Nu_t, Nu_b, $\langle T \rangle$, $\langle V_{rms} \rangle$, $V_{r\_md\_max}$, $V_{r\_md\_min}$, T_{md_max}, and T_{md_min} and their comparisons with previous studies when they are available. In addition to these averaged values, Table 6 also gives the time interval from t_1 to t_2 over which the averages and the standard deviations are

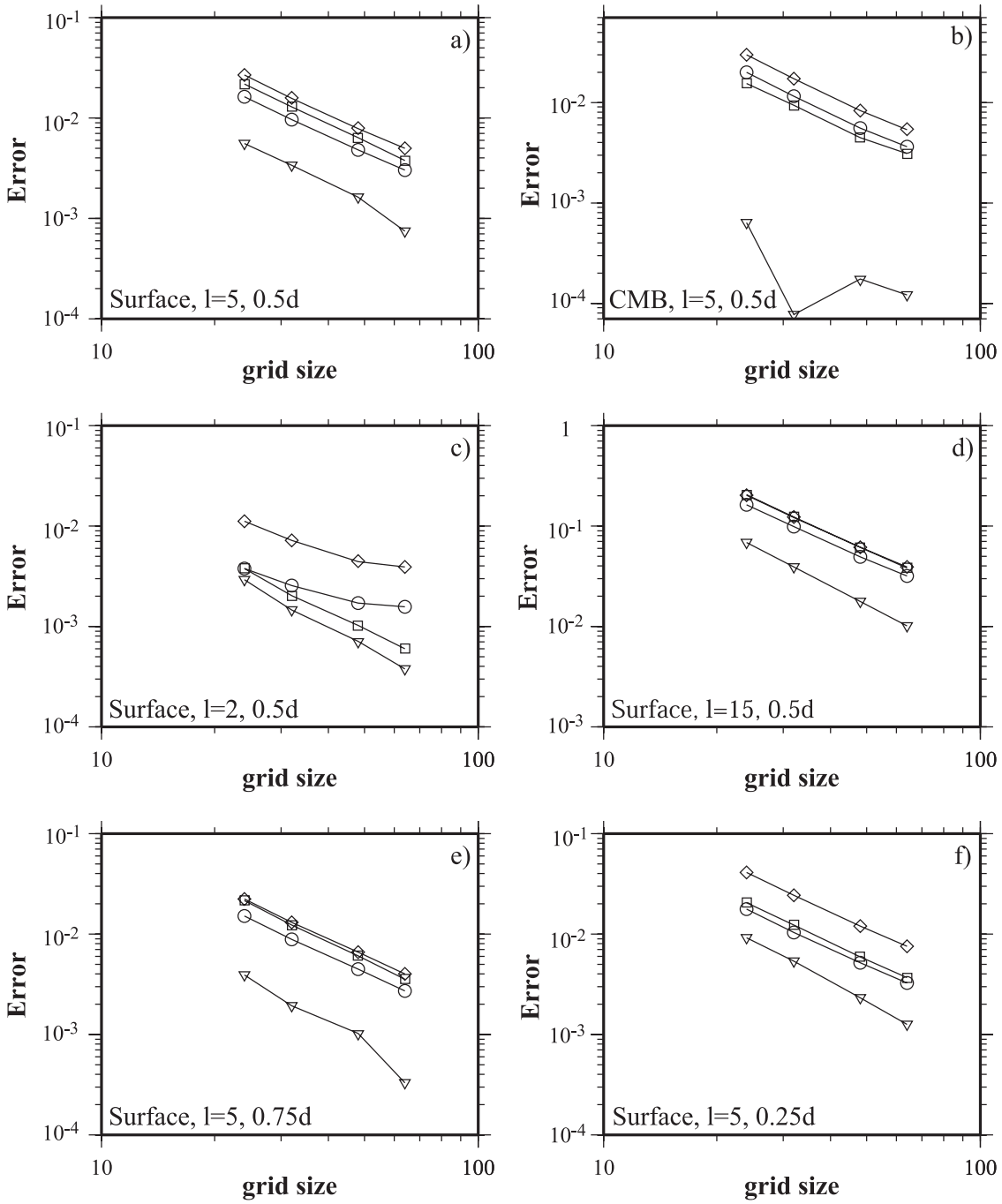

Figure 4. (a) Dependence of relative error on the number of elements in radial direction (i.e., resolution) for $l = 5$ surface response functions of topography (circles), geoid (diamonds), characteristic velocity (triangles), and divergence (squares) for the first set of calculations with the buoyancy at the depth of $0.5d$. (b) The same as Figure 4a but for CMB response functions. (c and d) The same as Figure 4a except for $l = 2$ and 15, respectively. (e and f) The same as Figure 4a except that the depths of the buoyancy are $0.75d$ and $0.25d$, respectively. Note that d is the thickness of the mantle.

computed. The results are at steady state, as demonstrated by the small standard deviations.

[69] Cases A1–A3 were published previously by *Stemmer et al.* [2006], *Ratcliff et al.* [1996a], and *Yoshida and Kageyama* [2004]. The results from CitcomS compare well with these previous studies (Table 6). For these cases, *Stemmer et al.* [2006] used numerical grids with 48 × (6 × 48 × 48)

Table 5. Convection Benchmark and Test Cases

Case	Style[a]	Ra	$\Delta\eta$	I.C.[b]	Resolution	Np[c]	Time Steps
A1	W	7×10^3	1	(3, 2)	12×32^3	–	10,000
A2	W	7×10^3	10	(3, 2)	12×32^3	–	15,000
A3	W	7×10^3	20	(3, 2)	12×32^3	–	11,000
A4	W	7×10^3	10^2	(3, 2)	12×32^3	–	30,000
A5	W	7×10^3	10^3	(3, 2)	12×32^3	–	31,000
A6	W	7×10^3	10^4	(3, 2)	12×32^3	–	110,000
A7	W	7×10^3	10^5	(3, 2)	12×32^3	–	70,000
A8	W	7×10^3	10^6	(3, 2)	12×32^3	–	76,000
A9	W	7×10^3	10^7	(3, 2)	12×32^3	–	65,000
B1	W	7×10^3	1	(4, 0) + (4, 4)	12×32^3	–	16,000
B2	W	7×10^3	20	(4, 0) + (4, 4)	12×32^3	–	14,000
B3	W	7×10^3	30	(4, 0) + (4, 4)	12×32^3	–	14,000
B4	W	7×10^3	10^2	(4, 0) + (4, 4)	12×32^3	–	18,000
B5	W	7×10^3	10^3	(4, 0) + (4, 4)	12×32^3	–	19,000
B6	W	7×10^3	10^4	(4, 0) + (4, 4)	12×32^3	–	50,000
B7	W	7×10^3	10^5	(4, 0) + (4, 4)	12×32^3	–	47,000
B8	W	7×10^3	10^6	(4, 0) + (4, 4)	12×32^3	–	41,000
B9	W	7×10^3	10^7	(4, 0) + (4, 4)	12×32^3	–	65,000
B9H	W	7×10^3	10^7	B9	12×48^3	–	25,000
B9HH	W	7×10^3	10^7	B9H	12×64^3	–	18,000
C1	W	10^5	1	(4, 0) + (4, 4)	12×48^3	–	35,000
C2	W	10^5	10	C1	12×48^3	–	30,000
C3	W	10^5	30	C1	12×48^3	–	35,000
C3H	W	10^5	30	C3	12×64^3	–	15,000
C4	W	10^5	100	C3	12×48^3	–	54,000
D1a	L	10^5	1	C1	12×48^3	15	14,000
D1b	L	10^5	1	C1	12×48^3	30	14,000
D1c	L	10^5	1	C1	12×64^3	15	22,000
D1d	L	10^5	1	C1	12×96^3	10	39,500
D1a_4RK	L	10^5	1	C1	12×48^3	15	14,000
D2a	L	10^5	30	C3	12×48^3	15	13,500
D2b	L	10^5	30	C3	12×64^3	15	18,500
D2a_4RK	L	10^5	30	C3	12×48^3	15	14,000

[a] "W" stands for whole mantle thermal convection models, while "L" is for layered mantle convection models. For all the "L" cases, the buoyancy number β is 1, and other parameters are given in text.

[b] I.C. represents the initial conditions. For spherical harmonic perturbations, (3, 2) stands for $l = 3$ and $m = 2$ and leads to tetrahedral symmetry planform of mantle convection, and (4, 0) + (4,4) stands for perturbations at two distinct wavelengths, one with $l = 4$ and $m = 0$ and the other with $l = 4$ and $m = 4$, and such perturbations lead to cubic symmetry planform. C1 means that the case used case C1's steady state temperature field as an initial condition. For cases B9H, B9HH, C3H, D1c, D1d, and D2b with higher resolution, initial temperature is taken from interpolated temperature from the steady state temperature for cases B9, B9H, and C3, respectively. More details for initial conditions are given in text.

[c] Np, only relevant for "L" cases, is the initial average number of tracers per element.

cells, and *Yoshida and Kageyama* [2004] used $102 \times (102 \times 204)$ cells, where the numbers inside and outside parentheses represent horizontal and radial grid points, respectively. *Ratcliff et al.* [1996a] used different resolutions for cubic and tetrahedral symmetry cases, as they considered the symmetry of these cases and did not compute models in a full sphere. For the tetrahedral cases in the work of *Ratcliff et al.* [1996a], the equivalent resolution is 32, 32, and 64 cells in radial, colatitude, and longitude directions, respectively. For cubic symmetry cases to be discussed later, the corresponding resolution is 32, 64, and 128, respectively.

3.2.1.2. Cases With Cubic Symmetry and its Variations

[70] For cubic symmetry cases with $Ra = 7 \times 10^3$, we use the initial condition similar to *Ratcliff et al.* [1996a]:

$$T(r,\theta,\phi) = \frac{r_b(r-r_t)}{r(r_b-r_t)} + \varepsilon_c \left[p_{40}(\theta,\phi) + \frac{5}{7}\cos(4\phi) p_{44}(\theta,\phi) \right] \cdot \sin\left[\frac{\pi(r-r_b)}{(r_t-r_b)} \right], \quad (47)$$

where $\varepsilon_c = 0.01$ and $\sin(m\varphi)$ is excluded. We computed cases with temperature dependent viscosity with $\Delta\eta$ of 1, 10, 20, 10^2, 10^3, 10^4, 10^5, 10^6,

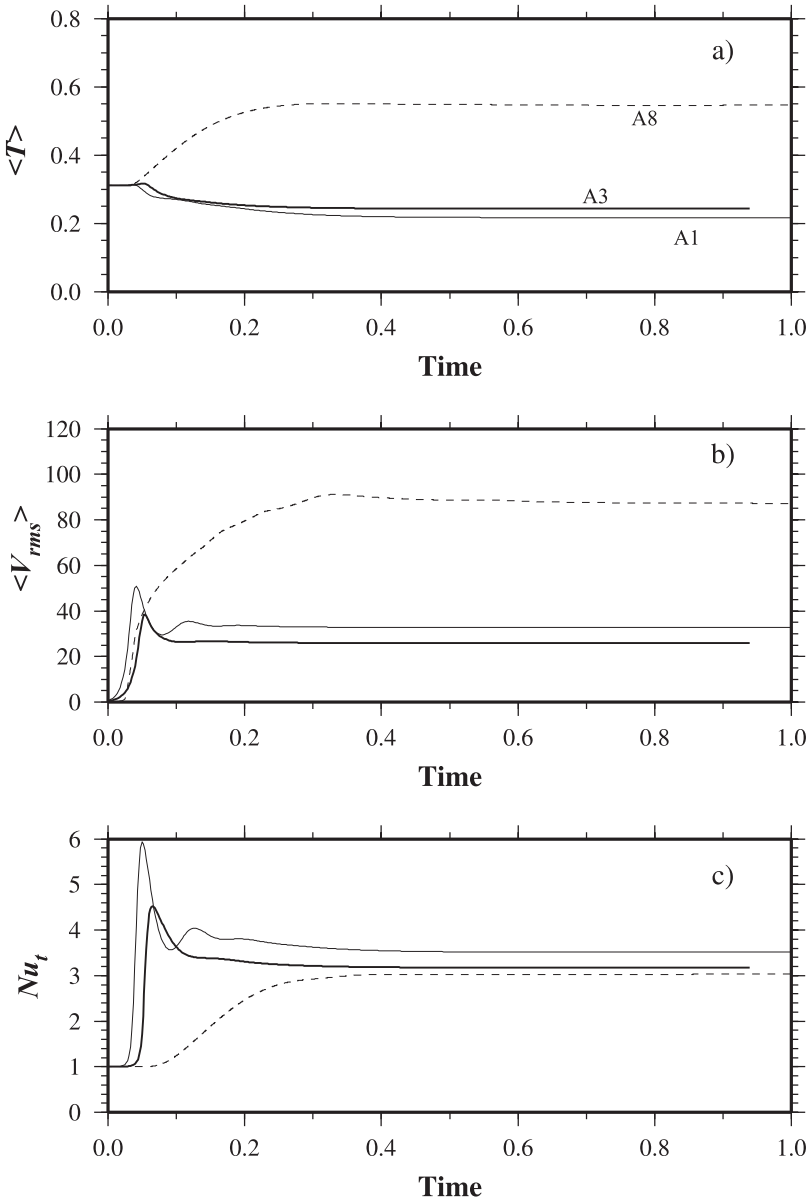

Figure 5. Time dependence of (a) volume-averaged temperature, $\langle T \rangle$, (b) root-mean-square (RMS) velocity, $\langle V_{rms} \rangle$, and (c) surface Nussult number, Nu_t, for cases A1 (thin solid line), A3 (thick solid line), and A8 (dashed line).

and 10^7 (Cases B1–B9 in Table 5 for definitions of all cases). The first three cases, B1–B3, can again be compared with previous studies. The first six cases (B1–B6) display cubic symmetry with six upwelling plumes (Figures 8a–8c for cases B1, B3, and B5). In contrast to the tetrahedral cases, the thermal structure in Case B6 with $\Delta\eta$ of 10^4 also shows the same cubic symmetry as cases with smaller viscosity contrast. The last three cases B7–B9 show stagnant lid convection that displays a large number of plumes (Figures 8d–8e for cases B7 and B9).

[71] Table 7 shows the output results and comparisons with previous studies when available in the same format as in Table 6. Cases B1–3 were published by *Stemmer et al.* [2006], *Ratcliff et al.* [1996a], and *Yoshida and Kageyama* [2004], and the results from CitcomS compare well with theirs. There is a small difference in *Nu* (i.e., heat flux) between the tetrahedral and cubic symmetry cases with the same Ra and $\Delta\eta$ (Tables 6 and 7), suggesting that *Nu* is weakly dependent on convective planform. For case B9, a resolution test with two sets of higher resolution: $12 \times (48 \times 48 \times 48)$

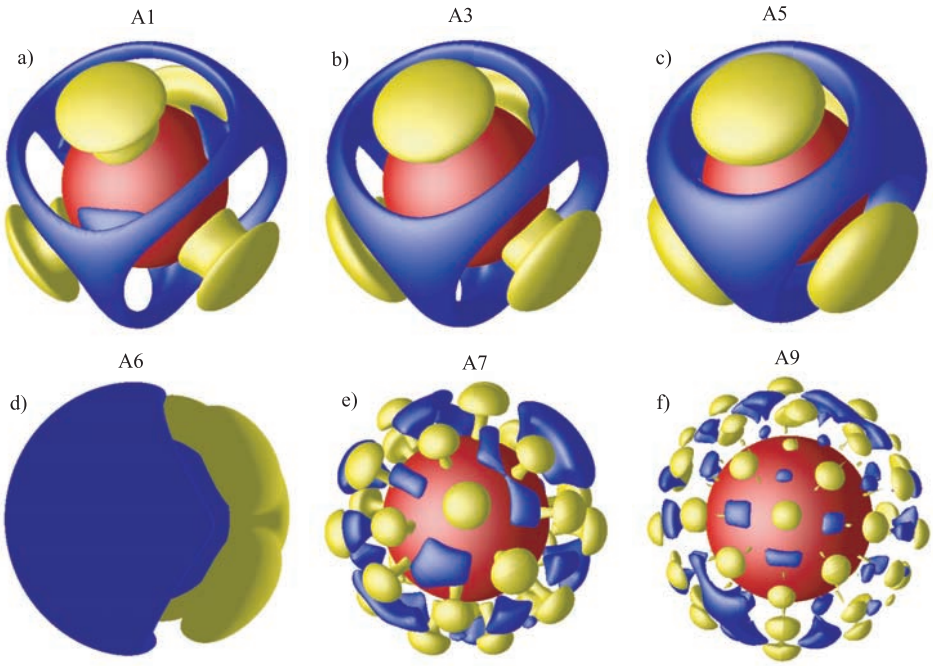

Figure 6. Representative steady state residual temperature $\delta T = T(r, \theta, \phi) - \langle T(r) \rangle$ for Cases (a) A1, (b) A3, (c) A5, (d) A6, (e) A7, and (f) A9, where $\langle T(r) \rangle$ is the horizontally averaged temperature. Blue and yellow isosurfaces are for δT equal to -0.15 and 0.15, respectively. The red sphere represents the core.

and $12 \times (64 \times 64 \times 64)$, indicates that our results are robust.

[72] For cases C1–4 with $Ra = 10^5$ and $\Delta\eta$ of 1, 10, 30, and 100 (Table 5), the steady state thermal structure also shows a cubic symmetry (Figures 8g–8i). However, due to the increased Ra, downwelling and upwelling plumes are thinner, compared with those from cases with smaller Ra. We used equation (47) as the initial condition only for case C1 with uniform viscosity. In order to preserve the cubic symmetry of the flow, the steady state temperature from case C1 is used as an initial condition for cases C2 and C3, and the steady state temperature from case C3 is used as initial condition for case C4 (Table 5). We found that if equation (47) is used as initial conditions for these temperature-dependent viscosity with $Ra = 10^5$, the planform with cubic symmetry does not develop and rather displays a large number of plumes.

[73] Table 8 shows the results from CitcomS for cases C1–C4 and comparisons with *Ratcliff et al.* [1996a] for cases C1–C3. While the results from CitcomS compares reasonably well with *Ratcliff et al.* [1996a], the differences are significantly larger than those for small Ra cases presented earlier. We think that the differences are probably caused by the resolution difference. *Ratcliff et al.* [1996a] used the same resolution (i.e., 32, 64, and 128 cells in radial, colatitude, and longitude directions, respectively) for all their cubic symmetry cases of different Ra. In addition, *Ratcliff et al.* [1996a] used steady state temperature from smaller Ra cases as initial conditions for higher Ra cases. We think that cases with $Ra = 10^5$ may require higher resolution. For case C3, we also performed a resolution study with case C3H of higher resolution (Table 5). For case C3H, the initial temperature was taken from an interpolated temperature from the steady state temperature of case C3. This resolution study shows that our results are well resolved (Table 7).

3.2.2. Thermochemical Convection

[74] An earlier study using CitcomS for thermochemical convection focused on the accuracy of tracer advection algorithm and conservation of total composition [*McNamara and Zhong*, 2004]. Here, we present test calculations that include additional outputs such as heat flux. For our thermochemical convection models, a dense layer with a density corresponding to a buoyancy number $B = 1$ is initially placed at the bottom of the mantle from the CMB to $r_{comp} = 0.775$, and there is no topography at the density interface. The initial

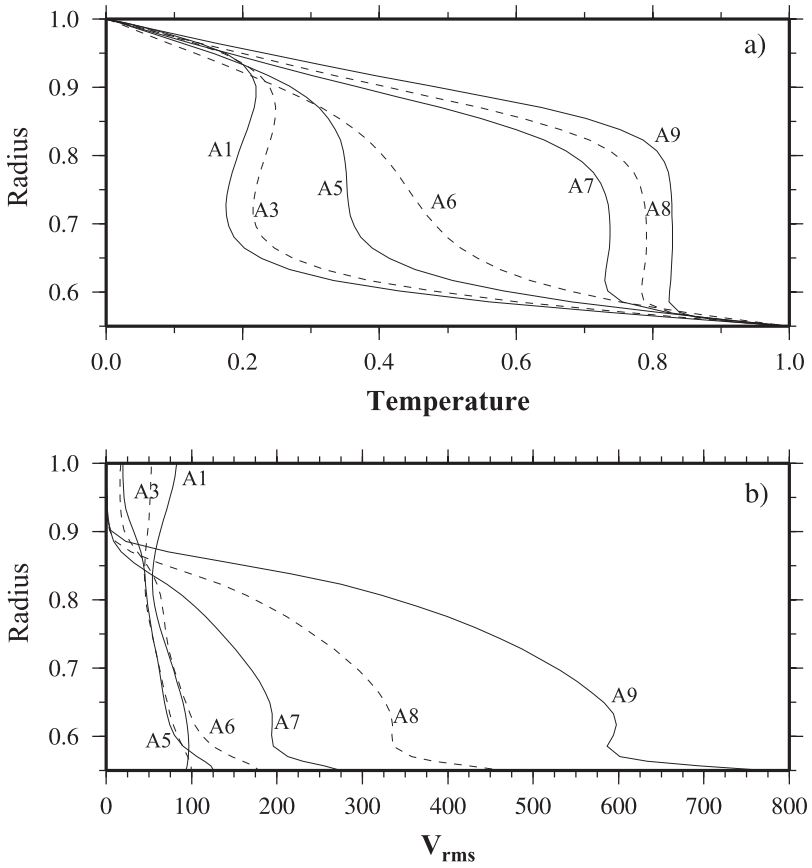

Figure 7. Radial dependence of horizontally averaged (a) temperature and (b) RMS velocity for cases A1, A3, A5, A6, A7, A8, and A9.

non-dimensional volume of the dense layer is 1.2526.

[75] For case D1a with uniform mantle viscosity of 1 (Table 5), initial temperature was taken from a steady state temperature for case C1 (Figure 8g). The averaged number of tracers per element is 15. Because of differences in element size, the number of tracers per element in the lower mantle is less than that for the upper mantle. We computed case D1a for 14,000 time steps. Figures 9a and 9b show the representative thermal and compositional fields after the solutions have reached a statistically steady state.

[76] For case D1a, the volume of the dense component decreases with time due to numerical errors, as indicated by the relative error in conserving the total volume of the dense component ε_V (the thin solid line in Figure 10a). However, the error is limited to less than 2% for this case. The volume of entrained dense component to the top layer C_e increases with time (the thin solid line in Figure 10b). At the end of the calculation, C_e is about 0.12, close to 10% of the initial volume of the dense layer. The time dependences of RMS velocity, $\langle V_{rms} \rangle$ (Figure 10c), and surface Nu (Figure 10d) suggest that this case reaches a statistically steady state. Similar to thermal convection cases, the time averaged steady state results of $\langle T \rangle$, $\langle V_{rms} \rangle$, Nu and other measurements are presented in Table 8.

[77] Cases D1b, D1c, and D1d are computed and they differ from case D1a only in having more particles and higher resolution, respectively (Table 5). These cases show nearly identical time dependence in $\langle V_{rms} \rangle$, and Nu, compared to those for case D1a (Figures 10c and 10d), indicating that case D1a is well resolved for these physical quantities. While the increased number of particles in case D1b does not affect the entrainment results nor conservation of the dense component, the increased resolution in cases D1c and D1d greatly reduces the entrainment and errors in conserving the total volume of the dense component (Figures 10a and 10b). This suggests that entrainment is more sensitive to numerical resolution and is not well resolved in these calculations, consistent

Table 6. Results for Cases With Tetrahedral Symmetry and its Variations[a]

Case	t_1	t_2	$\langle V_{rms} \rangle$	Nu_t	Nu_b	$\langle T \rangle$	T_{md_min}	T_{md_max}	$V_{r\_md\_min}$	$V_{r\_md\_max}$
A1	0.7	1.0	32.66(6e-4)	3.5126(2e-4)	3.4919(1e-5)	0.2171(2e-5)	0.01761(6e-6)	0.8976(3e-5)	−29.96(4e-3)	114.9(2e-3)
SHH			32.59	3.4864	3.4864					
RSZ			32.19	3.4423						
YK			32.09	3.4430						
A2	1.0	1.3	27.36(1e-4)	3.2674(1e-5)	3.2491(1e-5)	0.2360(3e-7)	0.02130(3e-6)	0.9090(2e-5)	−17.16(2e-3)	140.2(7e-3)
SHH			27.26	3.2398	3.2399					
RSZ			26.80	3.2337						
A3	0.6	0.9	25.85(1e-3)	3.1724(3e-4)	3.1548(1e-5)	0.2432(3e-5)	0.02324(9e-6)	0.9136(4e-6)	−15.01(2e-3)	148.2(2e-3)
SHH			25.73	3.1447	3.1450					
RSZ			25.69	3.1615						
YK			26.11	3.1330						
A4	1.5	2.0	23.11(3e-4)	2.9354(4e-5)	2.9205(3e-5)	0.2653(2e-6)	0.03321(4e-6)	0.9255(2e-4)	−10.74(2e-3)	171.3(0.1)
A5	1.0	1.5	22.90(3e-3)	2.5468(5e-4)	2.5352(4e-4)	0.3124(1e-5)	0.06951(3e-5)	0.9452(1e-3)	−6.972(0.1)	226.7(1.4)
A6	2.6	3.6	29.21(8e-2)	2.0414(4.1e-3)	2.0327(5.1e-3)	0.3511(1.3e-3)	0.1523(4e-4)	0.9603(2.0e-3)	−21.13(1.5)	298.4(3.8)
A7	1.2	1.7	50.21(8e-3)	2.7382(5e-4)	2.7431(6e-5)	0.5039(1e-4)	0.2701(2e-4)	0.9437(4e-4)	−23.98(0.09)	298.2(1.8)
A8	0.8	1.0	87.27(0.04)	3.0317(2.8e-3)	3.0685(3.4e-3)	0.5461(1e-4)	0.4838(3.1e-3)	0.9661(7e-4)	−47.11(0.20)	749.6(5.0)
A9	0.48	0.54	157.6(0.04)	3.5634(1.1e-3)	3.6076(1.1e-3)	0.5953(1e-4)	0.5713(9e-4)	0.9744(1e-4)	−125.3(0.18)	1399(1)

[a] Here t_1 and t_2 are the starting and ending times for computing the averages. Other symbols are defined in the text. The numbers in parentheses are standard deviations. SHH is *Stemmer et al.* [2006], RSZ is *Ratcliff et al.* [1996a], and YK is *Yoshida and Kageyama* [2004]. No standard deviations were given in these previous studies.

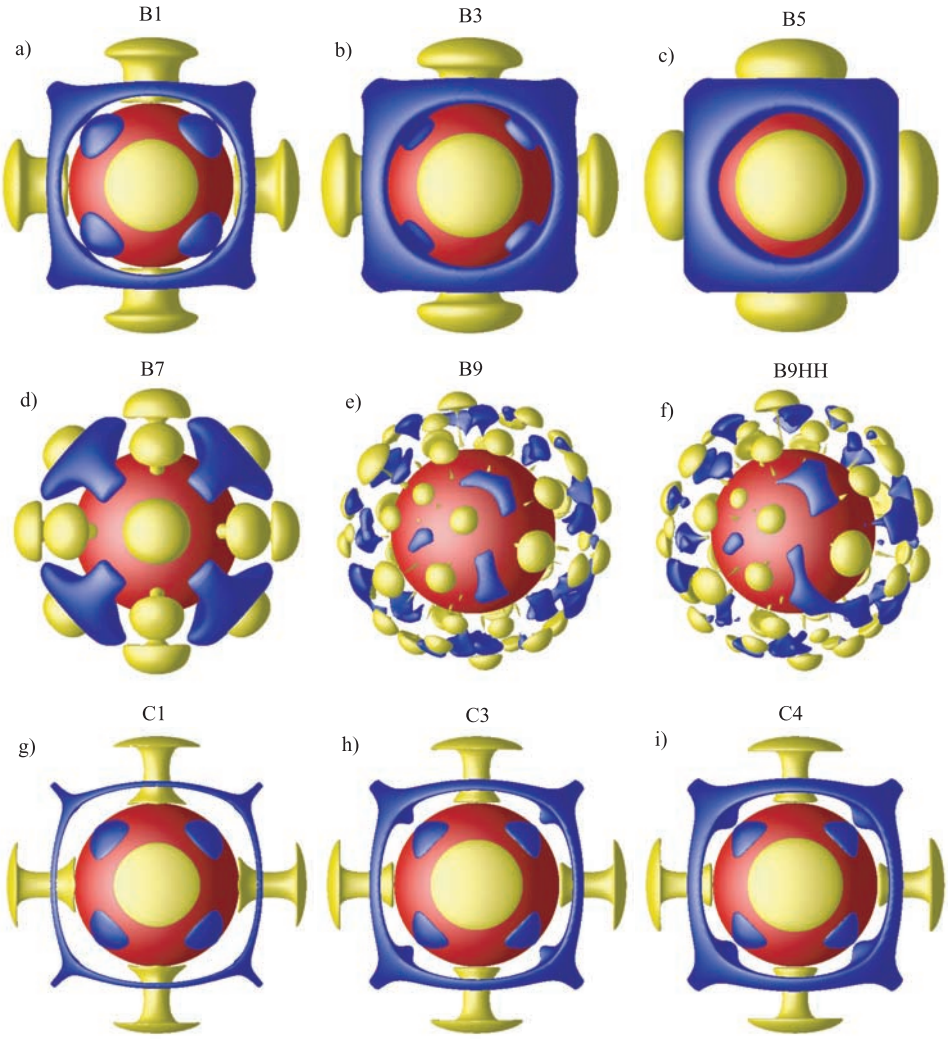

Figure 8. Representative steady state residual temperature for Cases (a) B1, (b) B3, (c) B5, (d) B7, (e) B9, (f) B9H, (g) C1, (h) C3, and (i) C4. Blue and yellow isosurfaces are for δT equal to -0.15 and 0.15, respectively.

with previous studies [*van Keken et al.*, 1997; *Tackley and King*, 2003; *McNamara and Zhong*, 2004].

[78] Radial dependences of horizontally averaged temperature, composition, and RMS velocity for cases D1a, D1c, and D1d at statistically steady states are shown in Figures 11a–11c, respectively. The temperature and composition plots clearly show two-layer convection with a compositional boundary in the middle of the mantle and three thermal boundary layers.

[79] Case D2a and its high resolution version case D2b employ a temperature-dependent viscosity with $\Delta\eta = 30$ (Table 5) but are otherwise same as cases D1a and D1c. Initial temperature field is taken from case C3. The averaged number of particles per element is 15 for both cases. The results are generally similar to those with uniform viscosity (see Figures 9, 10, and 11 and Table 8). A noticeable difference is that with temperature-dependent viscosity, convection in the bottom layer is more vigorous (Figure 11f). The averaged quantities from case D2a are well resolved, by comparing with those from high-resolution case D2b.

[80] For the two thermochemical cases with different numerical resolution (cases D1a, D1c, and D1d for the isoviscous case and cases D2a and D2b for variable viscosity case in Table 5), while all other measures are consistent (Figures 10 and 11 and Table 8), the largest difference caused by the resolution seems to be associated with maximum and minimum radial velocities at the midmantle depth (Table 8). This may be caused by the time-dependent nature of thermochemical convection

Table 7. Results for Cases With Cubic Symmetry and its Variations[a]

Case	t_1	t_2	$\langle V_{rms} \rangle$	Nu_t	Nu_b	$\langle T \rangle$	T_{md_min}	T_{md_max}	$V_{r\_md\_min}$	$V_{r\_md\_max}$
B1	1.2	1.7	31.09(1e-4)	3.6254(1e-5)	3.6016 (1e-5)	0.2176(6e-7)	0.02759(2e-6)	0.8654(5e-6)	−34.60(8e-4)	109.3(2e-4)
SHH			31.02	3.5982	3.5984					
RSZ			30.87	3.5806						
YK			30.52	3.5554						
B2	0.8	1.1	25.13(7e-5)	3.3721(2e-5)	3.3513(3e-6)	0.2527(2e-6)	0.03979(6e-7)	0.8912(4e-7)	−17.97(3e-4)	135.2(4e-4)
SHH			24.98	3.3423	3.3427					
RSZ			25.17	3.3663						
YK			25.39	3.3280						
B3	0.8	1.2	24.35(8e-5)	3.3162 (2e-5)	3.2960(4e-6)	0.2587(2e-6)	0.04222(1e-6)	0.8950(4e-7)	−16.37(3e-4)	139.0(5e-4)
SHH			24.20	3.2864	3.2869					
RSZ			24.57	3.1615						
B4	1.0	1.3	22.49(2e-5)	3.1278(6e-6)	3.1093(1e-6)	0.2797(4e-7)	0.05228(4e-6)	0.9072(6e-7)	−12.31(4e-4)	152.3(4e-4)
B5	0.8	1.0	22.29(2e-4)	2.6780(2e-5)	2.6635(6e-6)	0.3304(3e-6)	0.09614(3e-5)	0.9331(7e-6)	−7.404(1e-3)	195.4(0.01)
B6	1.2	1.6	29.94(4e-3)	2.3416(1e-4)	2.3322(4e-5)	0.3837(2e-5)	0.1772 (5e-4)	0.9593(1e-5)	−11.12(0.02)	300.4(0.05)
B7	0.75	1.05	51.01(0.02)	2.6698(1.0e-3)	2.6733(3e-4)	0.4878(1e-4)	0.3491 (3e-4)	0.9639(1e-4)	−21.19(0.07)	414.7(0.7)
B8	0.55	0.61	87.30(0.13)	3.0754(3e-4)	3.1073(1.9e-3)	0.5547(4e-5)	0.5146 (1.4e-3)	0.9660(9e-4)	−49.45(0.90)	682.2(6.3)
B9	0.54	0.58	158.7(0.1)	3.4753(1.5e-3)	3.5171(2.4e-3)	0.5899(4e-5)	0.5532(2.7e-3)	0.9874(5e-4)	−121.6(0.4)	1830.3(9.5)
B9H	0.52	0.53	152.4(6e-3)	3.5332(2e-4)	3.5785(2e-4)	0.5912(1e-5)	0.5518(6e-4)	0.9791(1e-4)	−115.9(0.01)	1814.7(3.6)
B9HH	0.568	0.578	150.1(0.03)	3.5463(1e-4)	3.5780(2e-4)	0.5915(1e-5)	0.5577(5e-4)	0.9736(7e-5)	−118.0(0.2)	1765.2(0.6)
C1	0.255	0.315	154.8(0.04)	7.8495(5.4e-3)	7.7701(1.0e-3)	0.1728(2e-4)	0.02281(7e-5)	0.9454(2e-5)	−261.5(0.3)	982.6(0.4)
RSZ			157.5	7.5669						
C2	0.48	0.55	122.1(0.06)	7.0968(5.9e-3)	7.0505(1.3e-3)	0.1908(3e-4)	0.02717(5e-5)	0.9474(3e-5)	−145.0(0.2)	1088.2(0.1)
RSZ			127.3	7.0913						
C3	0.52	0.57	109.1(0.04)	6.7572(4.4e-3)	6.7182(9e-4)	0.2011(2e-4)	0.02954(4e-5)	0.9503(2e-5)	−108.7(0.1)	1194.4(0.1)
RSZ			115.6	6.8655						
C3H	0.625	0.655	109.0(0.01)	6.7540(6e-4)	6.7240(3e-4)	0.2009(3e-5)	0.02973(6e-6)	0.9414(1.3e-5)	−108.7(0.01)	1183.3(0.1)
C4	0.825	0.925	98.90(0.02)	6.4803(1.9e-3)	6.4362(4e-4)	0.2168(1e-4)	0.03316(2e-5)	0.9563(3e-6)	−80.70(0.05)	1383.6(0.02)

[a]Note: See Table 6 for notations.

Table 8. Results for Thermochemical Models[a]

Case	$\langle V_{rms} \rangle$	Nu_t	Nu_b	$\langle T \rangle$	T_{md_min}	T_{md_max}	$V_{r\_md\_min}$	$V_{r\_md\_max}$	$\langle C \rangle$	$\langle C_e \rangle$
D1a	48.93(0.55)	3.402(0.027)	3.374 (0.035)	0.3051(6e-4)	0.0187(3e-3)	0.900(7e-3)	−79.6(9.0)	83.7(6.1)	1.2288(7e-4)	0.106(8e-3)
D1b	49.01(0.71)	3.409(0.031)	3.350(0.008)	0.3049(2e-3)	0.0182(2e-3)	0.908(2e-3)	−84.8(11)	99.9(7.2)	1.2309(9e-4)	0.113(0.01)
D1c	50.22(0.52)	3.499(0.028)	3.459(0.011)	0.3079(1e-3)	0.0175(2e-3)	0.914(5e-3)	−69.9(6.1)	92.6(4.3)	1.2350(9e-4)	0.074(6e-3)
D1d	50.03(0.26)	3.508(0.012)	3.488(0.007)	0.3098(1e-3)	0.0172(2e-3)	0.925(4e-3)	−55.0(3.2)	102(5.3)	1.2427(6e-4)	0.050(4e-3)
D1a_4RK	49.24(0.19)	3.421(0.026)	3.363(0.022)	0.3048(1e-3)	0.0203(2e-3)	0.892(6e-3)	−75.2(6.0)	79.3(6.5)	1.2297(5e-4)	0.114(1e-2)
D2a	50.53(0.18)	3.375(0.020)	3.336(0.015)	0.3736(6e-4)	0.0508(2e-3)	0.940(4e-3)	−45.3(3.7)	153.4(11)	1.2041(3e-3)	0.016(1e-3)
D2b	51.15(0.21)	3.421(0.008)	3.403(0.005)	0.3739(4e-4)	0.0570(5e-3)	0.941(3e-3)	−42.9(2.9)	120.2(8.2)	1.2183(3e-3)	0.012(1e-3)
D2a_4RK	50.50(0.31)	3.377(0.019)	3.344(0.017)	0.3733(7e-4)	0.0525(3e-3)	0.934(5e-3)	−47.1(4.2)	137.6(22)	1.2019(5e-3)	0.017(2e-3)

[a] Note: The starting and ending times for averaging, $t_1 = 0.49$, and $t_2 = 0.59$ for cases D1a, D1b, D1c, D1d, and D1a_4RK, and $t_1 = 0.23$, and $t_2 = 0.28$ for cases D2a, D2b, and D2a_4RK. $\langle C \rangle$ is the total volume of the dense component averaged between t_1 and t_2, and its initial value is 1.2526. See Table 6 for other notations.

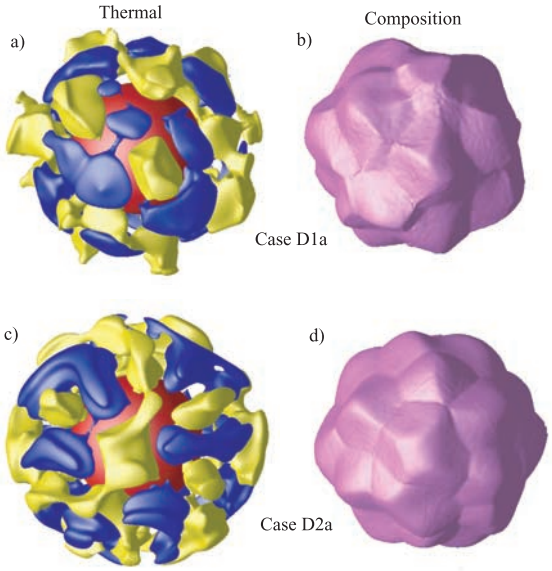

Figure 9. Representative steady state (a) residual temperature and (b) compositional interface for Case D1a and (c) residual temperature and (d) compositional interface for Case D2a. For the thermal structure plots, blue and yellow isosurfaces are for δT equal to −0.15 and 0.15, respectively.

(Figure 9) which may affect significantly the maximum and minimum flow velocities.

[81] Finally, we also computed two test cases D1a_4RK and D2a_4RK that use a fourth-order Runge-Kutte scheme for particle advection [e.g., *van Keken et al.*, 1997] but are otherwise identical to cases D1a and D2a (Table 5). We found that for these two test cases, the fourth-order Runge-Kutte scheme gave nearly identical results to those from the second-order predictor-corrector scheme (Table 8, Figure 10). The fourth-order Runge-Kutte scheme has been demonstrated to be important for particle-tracing related problems including accurately tracking the rapid evolution of compositional interface in Rayleigh-Taylor instability [e.g., *van Keken et al.*, 1997], although it is computationally significantly more expensive than the second-order predictor-corrector scheme used in most of our thermochemical convection calculations. There are two potential reasons that the second-order predictor-corrector scheme yields nearly identical results from the fourth-order Runge-Kutte scheme for our test cases. First, the time evolution of compositional field in thermochemical convection is relatively slow (e.g., compared with the exponential growth with time in Rayleigh-Taylor instability) and a robust second-order predictor-corrector method may be sufficient in capturing

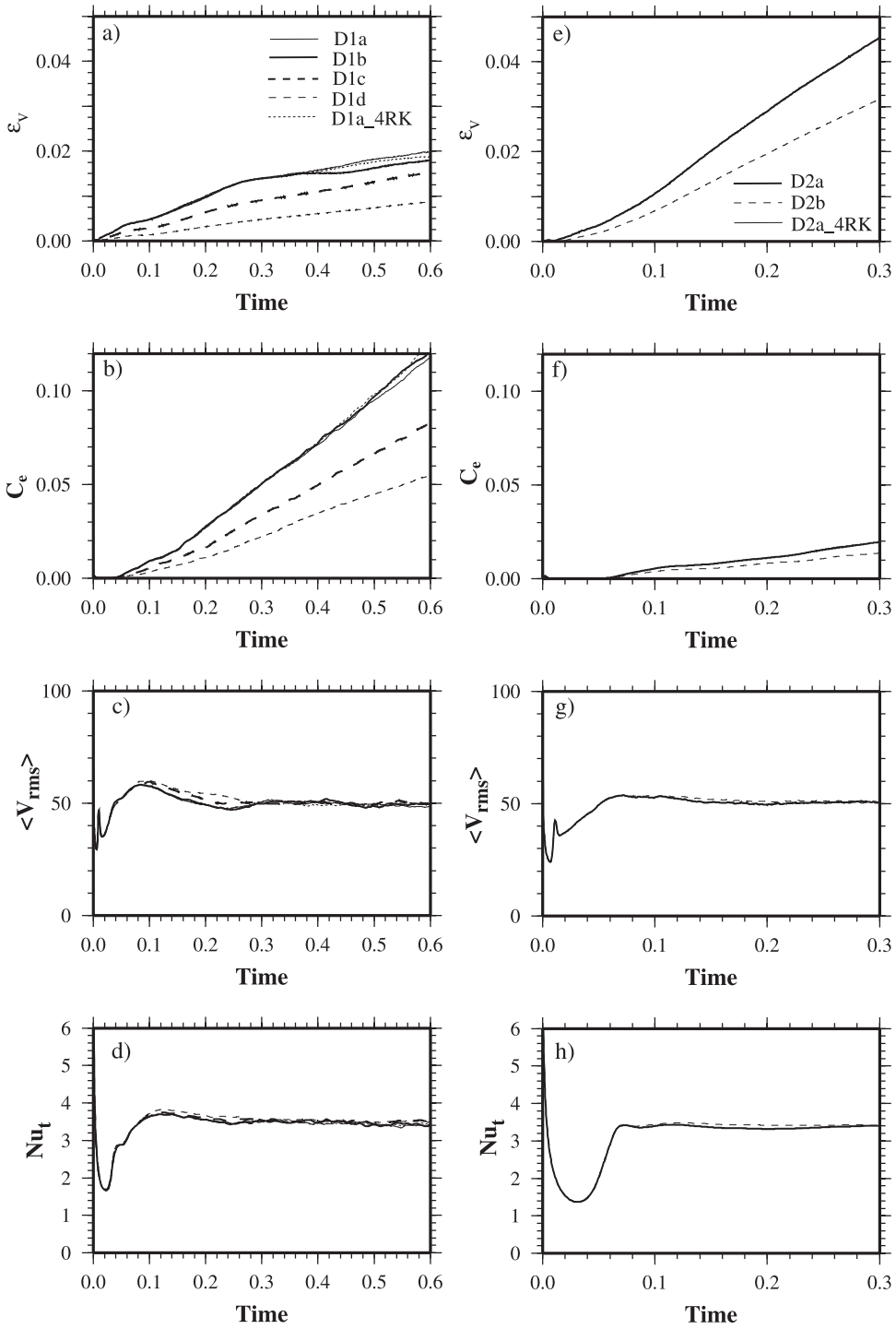

Figure 10. Time dependences of relative errors in conserving the (a) total volume of the dense component, ε_V, (b) entrained volume of the dense component, C_e, (c) RMS velocity, $\langle V_{rms} \rangle$, and (d) surface Nussult number, Nu_t, for cases D1a (thin solid lines), D1b (thick solid lines), D1c (thick dashed lines), D1d (thin dashed lines), and D1a_4RK (thin dotted lines). (e, f, g, and h) For cases D2a (thick solid lines), D2b (thin dashed lines), and D2a_4RK (thin solid lines). Notice that the lines for cases D2a and D2a_4RK are nearly identical.

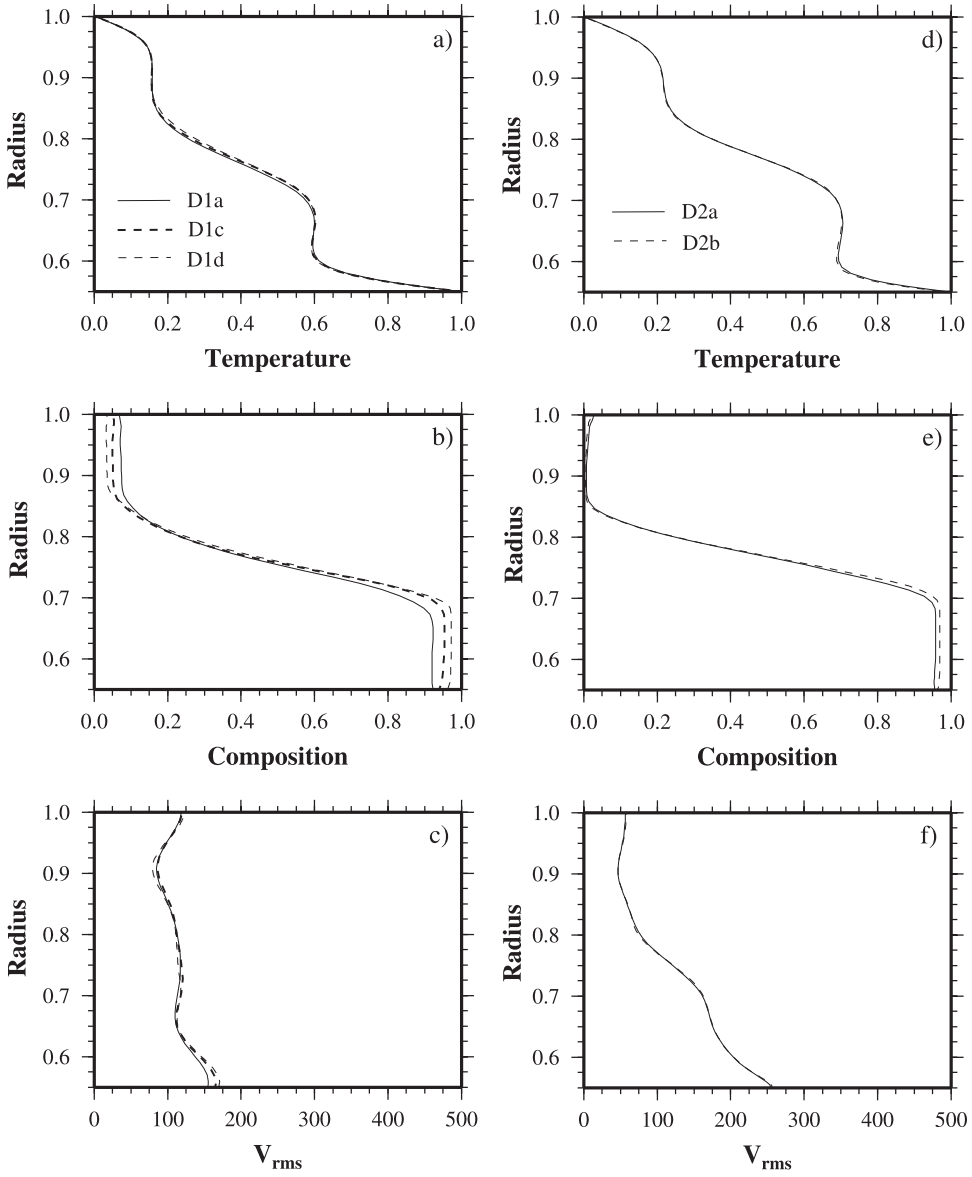

Figure 11. Radial dependence of horizontally averaged (a) temperature, (b) composition, and (c) RMS velocity for cases D1a (thin solid lines), D1c (thick dashed lines) and D1d (thin dashed lines). (d, e, and f) For cases D2a (solid lines) and D2b (dashed lines).

the time evolution. Second, most other numerical algorithms in CitcomS including the energy equation solver, and momentum equation solver are all second-order accurate, and this may reduce the benefit from the fourth-order accurate scheme. On the basis of our test calculations, we suggest that when computational cost is not a concern (e.g., in 2-D modeling), the fourth-order Runge-Kutte scheme is preferred. However, for 3-D thermochemical convection problems when computational cost is an important factor (note that particle tracing may account for 60–70% of computational time for most of our thermochemical convection calculations presented here), a robust second-order predictor-corrector method may also work reasonably well.

4. Conclusions and Discussions

[82] In this study, we presented benchmark and test calculations using the 3-D spherical finite element convection code CitcomS with two objectives: (1) to validate the accuracy of CitcomS and (2) to present comparison results for future studies. Two

classes of benchmark and test problems were studied: (1) the Stokes' flow and (2) thermal and thermochemical convection.

[83] For the Stokes' flow problem, we computed response functions of characteristic flow velocity, topography, and geoid at the surface and CMB at different spherical harmonic degrees (i.e., wavelengths) using CitcomS and we found that results from CitcomS agree well with those from analytic solutions using a propagator matrix method.

[84] For thermal and thermochemical convection problems, using CitcomS we calculated 24 cases with different model parameters including Rayleigh number (7000 or 10^5) and viscosity contrast due to temperature dependence (1 to 10^7). For each case, we computed (statistically) steady state results of time-averaged surface and CMB Nussult numbers, RMS velocity, averaged temperature, and maximum and minimum flow velocity and temperature at the midmantle depth and their standard deviation. For nine thermal convection cases with relatively small viscosity variations, comparisons with previously published results were possible and the comparisons show that CitcomS results are generally consistent with these previous studies with less than 1% difference. Where noticeable differences are observed at high Ra, resolution tests showed that our results are more robust. For thermochemical convection cases, in addition to outputs for thermal convection, we also quantified entrainment and the relative errors in conserving the volume of the dense component in the convection.

[85] In this study, we limited our calculations to steady state cases at relatively small *Ra* with no internal heat generation. We suggest that future benchmark studies for spherical mantle convection should consider fully time-dependent cases at high *Ra* with internal heating. Moreover, benchmark studies should be done for other problems including the effects of compressibility, phase change, and nonlinear rheology. However, these topics are beyond the scope of this paper.

Appendix A: Calculations of the Geoid and Topography for the Stokes' Flow

[86] Calculations of the geoid and topography for the Stokes' flow have been discussed extensively in the literature [*Hager and Richards*, 1989; *Zhang and Christensen*, 1993]. Here we briefly present the formulations and procedures that are used in this benchmark.

[87] Starting with the continuity and momentum equations (1) and (8) and the buoyancy force given in equation (41), and using R, η_r, $\sigma_0 g_0$, and $\sigma_0 g_0 R/\eta_r$ as scales for spatial coordinates, viscosity, stress (pressure), and velocity, respectively, equations (1) and (8) can be nondimensionalized to

$$\nabla \cdot \boldsymbol{u} = 0, \tag{A1}$$

$$-\nabla P + \nabla \cdot \left[\eta\left(\nabla \boldsymbol{u} + \nabla^T \boldsymbol{u}\right)\right] + \delta(r - r_0)\cos(m\phi) p_{lm}(\theta)\boldsymbol{e}_r = 0. \tag{A2}$$

For radially varying viscosity structure, these equations can be solved with a propagator matrix technique in a spherical harmonic spectral domain [e.g., *Hager and O'Connell*, 1981]. Since only cosine term is considered here in (A2), we may only need to include cosine terms in the analysis. The propagator matrix technique can directly yield solutions of reduced radial stress, σ_{rr}, and characteristic horizontal velocity, U, at the surface and CMB, for a given spherical harmonic degree l. Reduced radial stress, σ_{rr}, is used for determined the topography and geoid.

[88] Using $\sigma_0/\Delta\rho_t$ as a scale for surface topography, $\sigma_0/\Delta\rho_b$ for CMB topography, and $4\pi GR\sigma_0$ for gravitational potential, the dimensionless potentials and topography at the surface and CMB, for spherical harmonic degree l, are

$$s = -\sigma_{rr\_s} + q_s \varphi_s, \tag{A3}$$

$$b = \sigma_{rr\_b} + q_b \varphi_b, \tag{A4}$$

$$\varphi_s = \frac{1}{2l+1}\left[r_b\left(\frac{r_b}{r_t}\right)^{l+1} b + r_t s - r_0\left(\frac{r_0}{r_t}\right)^{l+1}\right], \tag{A5}$$

$$\varphi_b = \frac{1}{2l+1}\left[r_b b + r_t\left(\frac{r_b}{r_t}\right)^{l} s - r_0\left(\frac{r_b}{r_0}\right)^{l}\right], \tag{A6}$$

where equations (A3) and (A4) are derived from equations (28) and (33) and equations (A5) and (A6) are from equation (22), r_b, r_t, and r_0 are the dimensionless radial location of the CMB, surface, and the delta function buoyancy, respectively (note that $r_b = 0.55$ and $r_t = 1$), and

$$q_s = 4\pi GR\rho_m/g_0, \tag{A7}$$

$$q_b = 4\pi GR\Delta\rho_b/g_0, \tag{A8}$$

with the assumption that $\rho_m = \Delta\rho_t$.

[89] With the four equations (A3)–(A6), the dimensionless potentials and topography at the surface and CMB, s, b, φ_s, and φ_b can be solved for degree l. Once the dimensionless potentials are obtained, the dimensionless geoids at the surface and CMB can be determined with equation (34). In fact, if $4\pi GR\sigma_0/g_0$ is used as the geoid scale, then equations and (A6) give dimensionless geoids at the surface and CMB.

[90] For the Stokes' flow benchmark calculations presented in this study, parameters needed to compute q_s and q_b in equations (A7) and (A8) are given as follows. $\rho_m = 3300$ kg m^{-3}, $\Delta\rho_b = 5400$ kg m^{-3}, $R = 6370000$ m, $g_0 = 9.8$ m s^{-2}, and $G = 6.67 \times 10^{-11}$ m^3 kg^{-1} s^{-2}.

[91] To use CitcomS for benchmark calculations of response functions for the Stokes' flow problem, by comparing with equations (A1) and (A2), it is clear that we need to set $B = 0$ and $\xi Ra = 1$ in equations (11) and (12), and take T as in equation (44). CitcomS determines the CMB and surface reduced radial stresses on the numerical grid using a CBF method [*Zhong et al.*, 1993], after solving the flow velocity and pressure. We transform the reduced radial stresses to a spherical harmonic spectral domain using the spherical harmonic expansion (e.g., equation (19)). Equations (A3)–(A6) can then be used to determine dimensionless geoids and topography at the surface and CMB for CitcomS.

[92] The spherical harmonic expansion in CitcomS is implemented in two different methods. First, the surface integral for the expansion is done directly on the finite element grid over a spherical surface. Second, the field variable on the finite element grid is interpolated onto a set of regular θ and φ coordinates and then the surface integral is done on the regular θ and φ coordinates. In practice, we did not notice significant difference in performance between these two methods. The spherical harmonic expansion as discussed here may introduce dispersion errors at different spherical harmonics. However, for our calculations presented here, we found that such errors are generally much smaller than amplitude errors caused by numerical solutions of the governing equations.

Acknowledgments

[93] SZ was supported by NSF EAR-0711366 and David and Lucile Packard Foundation. AKM was supported by NSF-0510383. ET and MG were supported by NSF EAR-042271. We thank Scott King, Paul Tackley, and Peter van Keken for their constructive reviews and Teresa Lassak for going through equations and finding out two typos in two equations. Part of the calculations was performed on TACC's Parallel Supercomputer Ranger.

References

Atanga, J., and D. Silvester (1992), Iterative methods for stabilized mixed velocity-pressure finite elements, *Int. J. Numer. Methods Fluids*, *14*, 71–81, doi:10.1002/fld.1650140106.

Baumgardner, J. R. (1985), Three-dimensional treatment of convective flow in the Earth's mantle, *J. Stat. Phys.*, *39*, 501–511, doi:10.1007/BF01008348.

Becker, T. W. (2006), On the effect of temperature and strain-rate dependent viscosity on global mantle flow, net rotation, and plate-driving forces, *Geophys. J. Int.*, *167*, 943–957, doi:10.1111/j.1365-246X.2006.03172.x.

Becker, T. W. (2008), Azimuthal seismic anisotropy constrains net rotation of the lithosphere, *Geophys. Res. Lett.*, *35*, L05303, doi:10.1029/2007GL032928.

Bercovici, D. (2003), The generation of plate tectonics from mantle convection, *Earth Planet. Sci. Lett.*, *205*, 107–121, doi:10.1016/S0012-821X(02)01009-9.

Bercovici, D., G. Schubert, G. A. Glatzmaier, and A. Zebib (1989), 3-dimensional thermal-convection in a spherical-shell, *J. Fluid Mech.*, *206*, 75–104.

Billen, M. I., and G. Hirth (2007), Rheologic controls on slab dynamics, *Geochem. Geophys. Geosyst.*, *8*, Q08012, doi:10.1029/2007GC001597.

Blankenbach, B., et al. (1989), A benchmark comparison for mantle convection codes, *Geophys. J. Int.*, *98*, 23–38doi:10.1111/j.1365-246X.1989.tb05511.x.

Brooks, A. N. (1981), A Petrov-Galerkin finite element formulation for convection dominated flows, Ph.D. thesis, Calif. Inst. of Technol., Pasadena.

Bunge, H.-P., M. A. Richards, and J. R. Baumgardner (1996), Effect of depth-dependent viscosity on the planform of mantle convection, *Nature*, *379*, 436–438, doi:10.1038/379436a0.

Busse, F. H., et al. (1994), 3-D convection at infinite Prandtl number in Cartesian geometry - a benchmark comparison, *Geophys. Astrophys. Fluid Dyn.*, *75*, 39–59, doi:10.1080/03091929408203646.

Chandrasekhar, S. (1961), *Hydrodynamic and Hydromagnetic Stability*, Dover, New York.

Choblet, G., O. Cadek, F. Couturier, and C. Dumoulin (2007), OEDIPUS: A new tool to study the dynamics of planetary interiors, *Geophys. J. Int.*, *170*, 9–30, doi:10.1111/j.1365-246X.2007.03419.x.

Christensen, U. R. (1984), Convection with pressure- and temperature-dependent non-Newtonian rheology, *Geophys. J. R. Astron. Soc.*, *77*, 343–384.

Christensen, U. R., and D. A. Yuen (1984), The interaction of a subducting lithosphere with a chemical or phase boundary, *J. Geophys. Res.*, *89*(B6), 4389–4402.

Conrad, C. P., and C. Lithgow-Bertelloni (2006), Influence of continental roots and asthenosphere on plate-mantle coupling, *Geophys. Res. Lett.*, *33*, L05312, doi:10.1029/2005GL025621.

Dahlen, F. A., and J. Tromp (1998), *Theoretical Global Seismology*, Princeton Univ. Press, Princeton, N. J.

Forte, A. M., and W. R. Peltier (1994), The kinmatics and dynamics of poloidal-toroidal coupling in mantle flow: The importance of surface plates and lateral viscosity variations,

Adv. Geophys., *36*, 1–119, doi:10.1016/S0065-2687(08)60537-3.

Glatzmaier, G. A. (1988), Numerical simulations of mantle convection: Time-dependent, three-dimensional, compressible, spherical shell, *Geophys. Astrophys. Fluid Dyn.*, *43*, 223–264, doi:10.1080/03091928808213626.

Gurnis, M. (1989), A reassessment of the heat transport by variable viscosity convection with plates and lids, *Geophys. Res. Lett.*, *16*, 179–182, doi:10.1029/GL016i002p00179.

Hager, B. H., and R. J. O'Connell (1981), A simple global model of plate dynamics and mantle convection, *J. Geophys. Res.*, *86*, 4843–4878, doi:10.1029/JB086iB06p04843.

Hager, B. H., and M. A. Richards (1989), Long-wavelength variations in Earth's geoid: Physical models and dynamical implications, *Philos. Trans. R. Soc. London, Ser. A*, *328*, 309–327, doi:10.1098/rsta.1989.0038.

Harder, H., and U. R. Christensen (1996), A one-plume model of Martian mantle convection, *Nature*, *380*, 507–509, doi:10.1038/380507a0.

Harder, H., and U. Hansen (2005), A finite-volume solution method for thermal convection and dynamo problems in spherical shells, *Geophys. J. Int.*, *161*, 522–537, doi:10.1111/j.1365-246X.2005.02560.x.

Hughes, T. J. R. (2000), *The Finite Element Method*, 682 pp., Dover, New York.

Jaupart, C., and B. Parsons (1985), Convective instabilities in a variable viscosity fluid cooled from above, *Phys. Earth Planet Inter.*, *39*, 14–32, doi:10.1016/0031-9201(85)90112-8.

King, S. D., and B. H. Hager (1990), The relationship between plate velocity and trench viscosity in Newtonian and Power-Law subduction calculations, *Geophys. Res. Lett.*, *17*, 2409–2412, doi:10.1029/GL017i013p02409.

King, S. D., A. Raefsky, and B. H. Hager (1990), ConMan: Vectorizing a finite element code for incompressible two-dimensional convection in the Earth's mantle, *Phys. Earth Planet Inter.*, *59*, 195–207, doi:10.1016/0031-9201(90)90225-M.

McKenzie, D. P., J. M. Roberts, and N. O. Weiss (1974), Convection in the Earth's mantle: Towards a numerical solution, *J. Fluid Mech.*, *62*, 465–538, doi:10.1017/S0022112074000784.

McNamara, A. K., and S. Zhong (2004), Thermochemical structures within a spherical mantle: Superplumes or piles?, *J. Geophys. Res.*, *109*, B07402, doi:10.1029/2003JB002847.

Moresi, L., and M. Gurnis (1996), Constraints on the lateral strength of slabs from three-dimensional dynamic flow models, *Earth Planet. Sci. Lett.*, *138*, 15–28, doi:10.1016/0012-821X(95)00221-W.

Moresi, L. N., and V. S. Solomatov (1995), Numerical investigation of 2D convection with extremely large viscosity variation, *Phys. Fluids*, *7*, 2154–2164, doi:10.1063/1.868465.

Moresi, L. N., and V. S. Solomatov (1998), Mantle convection with a brittle lithosphere: Thoughts on the global tectonic styles of the Earth and Venus, *Geophys. J. Int.*, *133*, 669–682, doi:10.1046/j.1365-246X.1998.00521.x.

Moresi, L. N., S. J. Zhong, and M. Gurnis (1996), The accuracy of finite element solutions of Stokes' flow with strongly varying viscosity, *Phys. Earth Planet Inter.*, *97*, 83–94, doi:10.1016/0031-9201(96)03163-9.

O'Connell, R. J., C. W. Gable, and B. H. Hager (1991), Toroidal-poloidal partitioning of lithospheric plate motions, in *Glacial Isostasy, Sea-Level and Mantle Rheology*, edited by R. Sabadini, pp. 535–551, Kluwer Acad., Amsterdam.

Oldham, D., and J. H. Davies (2004), Numerical investigation of layered convection in a three-dimensional shell with application to planetary mantles, *Geochem. Geophys. Geosyst.*, *5*, Q12C04, doi:10.1029/2003GC000603.

Parmentier, E. M., C. Sotin, and B. J. Travis (1994), Turbulent 3-D thermal convection in an infinite Prandtl number, volumetrically heated fluid: Implications for mantle dynamics, *Geophys. J. Int.*, *116*, 241–251, doi:10.1111/j.1365-246X.1994.tb01795.x.

Ramage, A., and A. J. Wathen (1994), Iterative solution techniques for the Stokes and Navier-Stokes equations, *Int. J. Numer. Methods Fluids*, *19*, 67–83, doi:10.1002/fld.1650190106.

Ratcliff, J. T., G. Schubert, and A. Zebib (1996a), Steady tetrahedral and cubic patterns of spherical-shell convection with temperature-dependent viscosity, *J. Geophys. Res.*, *101*, 25,473–25,484, doi:10.1029/96JB02097.

Ratcliff, J. T., G. Schubert, and A. Zebib (1996b), Effects of temperature-dependent viscosity on thermal convection in a spherical shell, *Physica D*, *97*, 242–252, doi:10.1016/0167-2789(96)00150-9.

Richards, M. A., W. S. Yang, J. R. Baumgardner, and H.-P. Bunge (2002), Role of a low-viscosity zone in stabilizing plate tectonics: Implications for comparative terrestrial planetology, *Geochem. Geophys. Geosyst.*, *2*(8), 1026, doi:10.1029/2000GC000115.

Roberts, J. H., and S. J. Zhong (2006), Degree-1 convection in the Martian mantle and the origin of the hemispheric dichotomy, *J. Geophys. Res.*, *111*, E06013, doi:10.1029/2005JE002668.

Sidorin, I., M. Gurnis, and D. V. Helmberger (1999), Dynamics of a phase change at the base of the mantle consistent with seismological observations, *J. Geophys. Res.*, *104*, 15,005–15,023, doi:10.1029/1999JB900065.

Solomatov, V. S. (1995), Scaling of temperature- and stress-dependent viscosity convection, *Phys. Fluids*, *7*, 266–274, doi:10.1063/1.868624.

Stemmer, K., H. Harder, and U. Hansen (2006), A new method to simulate convection with strongly temperature-dependent and pressure-dependent viscosity in a spherical shell: Applications to the Earth's mantle, *Phys. Earth Planet Inter.*, *157*, 223–249, doi:10.1016/j.pepi.2006.04.007.

Tackley, P. J. (1993), Effects of strongly temperature-dependent viscosity on time-dependent, 3-dimensional models of mantle convection, *Geophys. Res. Lett.*, *20*, 2187–2190, doi:10.1029/93GL02317.

Tackley, P. J. (1998), Three-dimensional simulations of mantle convection with a thermo-chemical basal boundary layer: D, in *The Core-Mantle Boundary Region*, *Geodyn. Ser.*, vol. 28, edited by M. Gurnis et al., pp. 231–253, AGU, Washington, D. C.

Tackley, P. J. (2000), Self-consistent generation of tectonic plates in time-dependent, three-dimensional mantle convection simulations. 1. Pseudoplastic yielding, *Geochem. Geophys. Geosyst.*, *1*(8), 1021, doi:10.1029/2000GC000036.

Tackley, P. J., and S. D. King (2003), Testing the tracer ratio method for modeling active compositional fields in mantle convection simulations, *Geochem. Geophys. Geosyst.*, *4*(4), 8302, doi:10.1029/2001GC000214.

Tackley, P. J., D. J. Stevenson, G. A. Glatzmeir, and G. Schubert (1993), Effects of an endothermic phase transition at 670 km depth on spherical mantle convection, *Nature*, *361*, 137–160, doi:10.1038/361699a0.

Travis, B. J., C. Anderson, J. Baumgardner, C. W. Gable, B. H. Hager, R. J. O'Connell, P. Olson, A. Raefsky, and G. Schubert (1990), A benchmark comparison of numerical-methods for infinite Prandtl number thermal-convection in 2-dimensional Cartesian geometry, *Geophys.*

Astrophys. Fluid Dyn., *55*, 137–160, doi:10.1080/03091929008204111.

van Hunen, J., S. J. Zhong, N. M. Shapiro, and M. H. Ritzwoller (2005), New evidence for dislocation creep from 3-D geodynamic modeling the Pacific upper mantle structure, *Earth Planet. Sci. Lett.*, *238*, 146–155, doi:10.1016/j.epsl.2005.07.006.

van Keken, P. E., and S. J. Zhong (1999), Mixing in a 3D spherical model of present day mantle convection, *Earth Planet. Sci. Lett.*, *171*, 533–547, doi:10.1016/S0012-821X(99)00181-8.

van Keken, P. E., S. D. King, H. Schmeling, U. R. Christensen, D. Neumeister, and M.-P. Doin (1997), A comparison of methods for the modeling of thermochemical convection, *J. Geophys. Res.*, *102*, 22,477–22,496, doi:10.1029/97JB01353.

Yoshida, M., and A. Kageyama (2004), Application of the Yin-Yang grid to a thermal convection of a Boussinesq fluid with infinite Prandtl number in a three-dimensional spherical shell, *Geophys. Res. Lett.*, *31*, L12609, doi:10.1029/2004GL019970.

Yoshida, M., Y. Iwase, and S. Honda (1999), Generation of plumes under a localized high viscosity lid on 3-D spherical shell convection, *Geophys. Res. Lett.*, *26*, 947–950.

Young, R. E. (1974), Finite-amplitude thermal convection in a spherical shell, *J. Fluid Mech.*, *63*, 695–721, doi:10.1017/S0022112074002151.

Zhang, S., and U. Christensen (1993), Some effects of lateral viscosity variations on geoid and surface velocities induced by density anomalies in the mantle, *Geophys. J. Int.*, *114*, 531–547, doi:10.1111/j.1365-246X.1993.tb06985.x.

Zhang, S., and D. A. Yuen (1995), The influences of lower mantle viscosity stratification on 3-D spherical-shell mantle convection, *Earth Planet. Sci. Lett.*, *132*, 157–166, doi:10.1016/0012-821X(95)00038-E.

Zhong, S. J. (2001), Role of ocean-continent contrast and continental keels on Plate motion, net rotation of lithosphere and the geoid, *J. Geophys. Res.*, *106*, 703–712, doi:10.1029/2000JB900364.

Zhong, S. J., and G. F. Davies (1999), Effects of plate and slab viscosities on geoid, *Earth Planet. Sci. Lett.*, *170*, 487–496, doi:10.1016/S0012-821X(99)00124-7.

Zhong, S. J., and M. Gurnis (1993), Dynamic feedback between an non-subducting raft and thermal convection, *J. Geophys. Res.*, *98*, 12,219–12,232, doi:10.1029/93JB00193.

Zhong, S. J., and M. Gurnis (1996), Incorporation of fault-bound plates in three-dimensional models of mantle flow, *Nature*, *383*, 245–247, doi:10.1038/383245a0.

Zhong, S. J., and B. H. Hager (2003), Entrainment of a dense layer by thermal plumes, *Geophys. J. Int.*, *154*, 666–676, doi:10.1046/j.1365-246X.2003.01988.x.

Zhong, S. J., M. Gurnis, and G. Hulbert (1993), Accurate determination of surface normal stress in viscous flow from a consistent boundary flux method, *Phys. Earth Planet. Inter.*, *78*, 1–8, doi:10.1016/0031-9201(93)90078-N.

Zhong, S. J., M. Gurnis, and L. N. Moresi (1998), The role of faults, nonlinear rheology, and viscosity structure in generating plates from instantaneous mantle flow models, *J. Geophys. Res.*, *103*, 15,255–15,268, doi:10.1029/98JB00605.

Zhong, S. J., M. T. Zuber, L. N. Moresi, and M. Gurnis (2000), Role of temperature dependent viscosity and surface plates in spherical shell models of mantle convection, *J. Geophys. Res.*, *105*, 11,063–11,082, doi:10.1029/2000JB900003.

Zhong, S. J., N. Zhang, Z. X. Li, and J. H. Roberts (2007a), Supercontinent cycles, true polar wander, and very long-wavelength mantle convection, *Earth Planet. Sci. Lett.*, *261*, 551–564, doi:10.1016/j.epsl.2007.07.049.

Zhong, S. J., D. A. Yuen, and L. N. Moresi (2007b), Numerical methods in mantle convection, in *Treatise in Geophysics*, vol. 7, edited by G. Schubert, pp. 227–252, Elsevier, Amsterdam.